PONTIFICIA UNIVERSIDAD CATÓLICA DEL PERÚ

ESCUELA DE POSGRADO

EVALUATION OF SHEAR WAVE SPEED MEASUREMENTS USING CRAWLING WAVES SONOELASTOGRAPHY AND SINGLE TRACKING LOCATION ACOUSTIC RADIATION FORCE IMPULSE IMAGING

By

Juvenal Ormachea Quispe

Thesis submitted in partial fulfillment of the requirements for the degree of

Master in Digital Signal and Image Processing

in the Graduate School of the Pontificia Universidad Católica del Perú.

Thesis Supervisors: Benjamím Castañeda Aphán and Kevin J. Parker

Examining commitee members:

Paul Rodríguez Valderrama

Roberto J. Lavarello Montero

Lima, Perú

April, 2015

Abstract

Many pathological conditions are closely related with an increase in tissue stiffness. For many years, experts performed manual palpation in order to measure elasticity changes, however, this method can only be applied on superficial areas of the human body and provides crude stiffness estimation. Elastography is a technique that attempts to characterize the elastic properties of tissue in order to provide additional and useful information for clinical diagnosis. For more than twenty years, different research groups have developed various elastography modalities with a strong interest for quantitative images during the last decade. Recently, comparative studies among different elastographic techniques have been performed in order to better characterize biomaterials, to cross-validate several shear wave elastographic modalities and to study the factors that influence their precision and accuracy. This comparison works may contribute to achieve standardization in quantitative elastography and their use in commercial equipment for their application in human patients. However, there is still a limited literature in the field of quantitative elastography modalities comparisons.

This thesis focuses on the comparison between two elastographic techniques: crawling wave sonoelastography (CWS) and single tracking location-acoustic radiation force impulse (STL-ARFI). The comparison shows the estimation of the shear wave speed (SWS), lateral resolution, contrast and contrast-to-noise ratio (CNR) in homogeneous and inhomogeneous phantoms using both techniques. The SWS values obtained with both modalities are validated with mechanical measurements that are considered as ground truth. The SWS results for the three different homogeneous phantoms (10%, 13%, and 16% gelatin concentrations), show good agreement between CWS, STL-ARFI and mechanical measurements as a function of frequency. The maximum accuracy errors obtained with CWS were 2.52%, 1.63% and 2.26%. For STL-ARFI, the maximum errors were 6.22%, 5.63% and 4.08% for the 10%,13% and 16% gelatin phantom respectively. For lateral resolution, contrast and CNR estimated in the inhomogeneous phantoms, it can be seen that for vibration frequencies higher than 340 Hz, CWS presents better results than the obtained with STL-ARFI using distances between the push beams (Δx) higher than 4 mm. However, using these vibration frequencies will not be feasible for *in vivo* tissues due to attenuation problems. It that sense, for lower vibration frequencies than 300 Hz and Δx among 3 mm and 6 mm, comparable lateral resolution, contrast and CNR was obtained. Finally, the results of this study contribute to the data currently available for comparing elastographic techniques. Moreover, the methodology implemented in this document may be helpful for future standardization for different elastographic modalities.

A mis queridos padres por su comprensión, cariño y apoyo incondicional.

Contents

List of Figures

List of Tables

Chapter 1

Introduction

Many pathological conditions are closely related with an increase in tissue stiffness [5]. For hundreds of years, experts have performed manual palpation in order to measure elasticity changes. However, this method can only be applied on superficial areas of the human body and provides a crude estimation of tissue stiffness. Elastography is a technique that attempts to characterize the elastic properties of tissue in order to provide additional and useful information for clinical diagnosis [5]. For more than twenty years, different research groups have developed qualitative and quantitative elastography modalities. As a result, several techniques, mostly based on ultrasound but also on magnetic resonance imaging and optical coherence tomography, have been proposed and applied to a number of clinical applications such as cancer diagnosis (prostate, breast, liver), hepatic fibrosis staging, early detection of renal pathology, focal thyroid lesions characterizations, arterial plaque evaluation, wall stiffness measurement in arteries thrombosis evaluation in veins, and many others [3]. Recently, various groups have performed comparative studies among different elastographic techniques in order to characterize biomaterials [6, 7], to cross-validate several shear wave elastographic modalities [7, 8] and to study the factors that influence their precision and accuracy [8]. These comparisons evaluated the shear wave speed (SWS) generated in the medium, the shear modulus, or the Youngs modulus. Some of these comparisons validated their work using mechanical testing to evaluate elastic properties, or a rheometer to measure the linear viscoelasticity in the materials [6, 9]. Gennisson et al. [9], tried to show that supersonic shear imaging (SSI) has better potential than transient elastography (TE) for materials characterization and highlighted the need to extend SSI for viscoelastic properties estimation. TE and SSI have also been applied for the shear modulus assessment of thin-layered phantoms [7]. Since thin-layered phantoms can simulate arteries, skin or corneal tissues. Both techniques presented similar shear wave speed estimation even though they use different vibration sources. Fromageau et al. [6] made a characterization for polyvinyl alcohol cryogel (PVA-C) phantoms using mechanical tests and two different elastographic modalities: Quasistatic elastography and TE. Both modalities showed good correspondence with mechanical tests. Latorre-Ossa et a. [10], used static elastography and shear wave elastography (SWE) for nonlinear shear modulus estimation in gelatin-agar phantoms and beef liver samples. Static elastography and SWE measure the local strain and the SWS value, respectively. With this information, it was possible to recover the local Landau co-

efficient characterizing the shear nonlinearity of soft tissues. Oudry et al.[11] measured the elastic properties of tissue mimicking phantoms using four different quantitative modalities: quasi-static compression, dynamic mechanical analysis, vibration-controlled transient elastography and hyper-frequency viscoelastic spectroscopy. Their results suggest a bias in elastic property measurement which varies with systems and highlight the difficulty in finding a reference method to assess the elastic properties of phantoms. Thus, the authors in [11] showed that comparison among measurement devices is difficult and special precautions must be taken to study the elastic properties of phantoms. Furthermore, Oudry et al. claimed that there is still a need to perform additional studies to determine the source of measurement variations. In that sense, the work presented in [11] keep open the question: how can one choose a reference method to assess the elastic properties of model materials? Therefore, the literature for comparison quantitative elastographic methods contributes to the validation and standardization of different elastographic techniques. Nevertheless, there is still a lack of comparison studies using quantitative elastographic techniques based on mechanical vibration external forces like vibroacoustography or quantitative sonoelastography and quantitative elastographic techniques based on acoustic radiation force like SSI, SWE or single tracking location.

1.1 Objectives of the thesis

This thesis focuses on the comparison between two quantitative techniques with different vibration sources that have not been characterized together in the past: crawling wave sonoelastography (CWS) and single tracking location-acoustic radiation force impulse (STL-ARFI). The comparison shows the estimation of the shear wave speed, contrast, contrast-to-noise ratio (CNR) and spatial resolution in homogeneous and inhomogeneous phantoms using both techniques. The SWS values obtained with both modalities are validated with mechanical measurements (MM) that work as ground truth

1.2 Organization: outline

The rest of the document is organized as follows: Chapter II reviews the theory related to mechanical measurements and elastographic modalities based on mechanical forces and acoustic radiation forces. Chapter III introduces the materials for experiments and methods for the SWS, contrast, CNR and spatial resolution estimation. Chapter IV presents the experimental results. Chapter V contains the discussion of our experimental results. Finally, Chapter VI presents the conclusions.

Chapter 2

Theory

2.1 Mechanical Measurements

2.1.1 The Kelvin-Voigt Fractional Derivative (KVFD) model

The KVFD model is a generalization of the Kelvin-Voigt (KV) model. Kumar et al. [12] found that the KVFD model provided a better fit than the KV and Maxwell models to experimental data from tissue-mimicking phantoms. In the KV model, stress in the dashpot is equal to the first derivative with respect to time of the strain. The KVFD model consists of a spring in parallel with a fractional derivative dashpot (See Fig. 2.1). The stress in the dashpot is equal to the fractional derivative of the strain. The KVFD model contains three parameters: E_0, η and α, where E_0, refers to the relaxed elastic constant, η refers to the viscoelastic parameter, and α is the order of fractional derivative. In [1], Zhang et al. shows the relationship between stress and strain parameters in the KVFD model, which is given by the following equations:

$$\sigma(t) = E_0\epsilon(t) + \eta D^{\alpha}[\epsilon(t)], \tag{2.1}$$

where σ is the stress, ϵ is the strain, t is time and $D^{\alpha}[]$ is the fractional derivative operator defined by:

$$D^{\alpha}[x(t)] = \frac{1}{\Gamma(1-\alpha)} \int_0^t \frac{x'(\tau)}{(t-\tau)^{\alpha}} \mathrm{d}\tau, \tag{2.2}$$

where Γ is the gamma function. Additionally, for the KVFD model $0< \alpha <1$

2.1.2 Stress Relaxation

Stress relaxation is one of the characteristics of soft tissue. When a material with viscoelastic properties is held at constant strain, the stress decreases with time. To develop a form of the relaxation function, the applied strain is modeled as a ramp of duration T_0 followed by

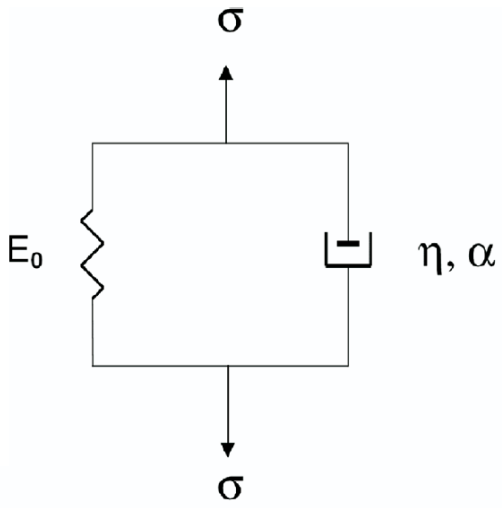

Figure 2.1: A diagram of the Kelvin-Voigt fractional derivative (KVFD) model [1].

a hold period of constant strain ϵ_0. So the strain function is:

$$\epsilon(t) = \begin{cases} \frac{t}{T_0} & : 0 < t < T_0 \\ \epsilon_0 & : t \geq T_0, \end{cases} \tag{2.3}$$

By taking the Laplace transform of equations (2.2) and (2.3), equations (2.4) and (2.5) can obtain:

$$\sigma(s) = E_0\epsilon(s) + \eta s^{\alpha}\epsilon(s), \tag{2.4}$$

$$\epsilon(s) = \frac{\epsilon_0}{s^2 T_0}\left(1 - e^{s}T_0\right), \tag{2.5}$$

where s is the Laplace domain variable. Using (2.4) and (2.5), $\sigma(s)$ can be described as:

$$\sigma(s) = E_0\frac{\epsilon_0}{s^2 T_0}\left(1 - e^{sT_0}\right) + \eta\frac{\epsilon_0}{s^{2-\alpha}T_0}\left(1 - e^{sT_0}\right), \tag{2.6}$$

Then, the inverse Laplace transform is applied to (2.6) and compared with (2.1)

$$\sigma(t) = E_0\frac{\epsilon_0}{T_0}\left(tu(t) - (t - T_0)u(t - T_0)\right) + \eta\frac{\epsilon_0}{\Gamma(2-\alpha)T_0}\left(t^{1-\alpha}u(t) - (t - T_0)^{1-\alpha}u(t - T_0)\right), \tag{2.7}$$

where $u(t)$ is the unit step function. Therefore, during the hold period ($t \geq T_0$) of the stress relaxation curve, the response of a material exhibiting KVFD behavior is:

$$\sigma(t) = E_0\epsilon_0 + \eta\frac{\epsilon_0}{\Gamma(2-\alpha)T_0}\left(t^{1-\alpha} - (t - T_0)^{1-\alpha}\right), \tag{2.8}$$

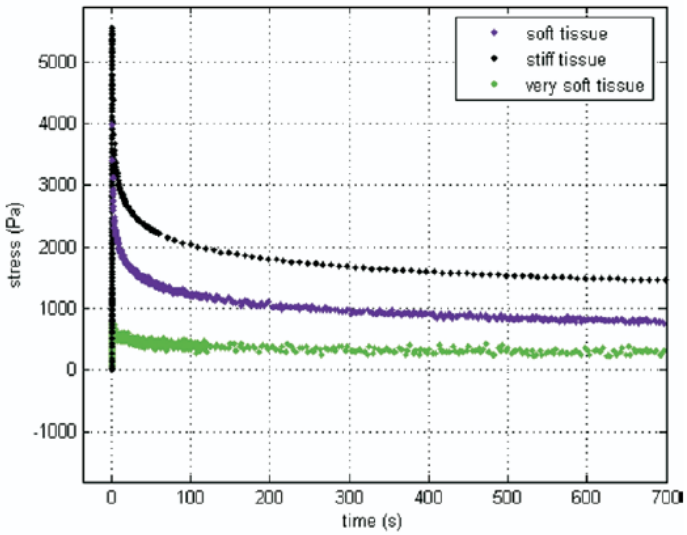

Figure 2.2: Typical stress relaxation curves obtained from different soft tissues [1].

2.1.3 Frequency response

Frecuency domain response can be obtained by taking the Fourier transform of equation (2.1)

$$\sigma(\omega) = E_0\epsilon(\omega) + \eta(j\omega)^\alpha\epsilon(\omega), \tag{2.9}$$

where ω=$2\pi f$ is the radian frequency and $j = \sqrt{-1}$ The complex modulus is obtained as a function of frequency

$$E^* = \frac{\sigma(f)}{\epsilon(f)} = \left[E_0 + \eta\cos\left(\frac{\pi\alpha}{2}\right)(2\pi f)^\alpha\right] + j\left[\eta\sin\left(\frac{\pi\alpha}{2}\right)(2\pi f)^\alpha\right], \tag{2.10}$$

From (2.10) we can get the storage modulus, $E'(f)$, and the loss modulus $E''(f)$

$$E'(f) = E_0 + \eta\cos\left(\frac{\pi\alpha}{2}\right)(2\pi f)^\alpha, \tag{2.11}$$

$$E'' = \eta\sin\left(\frac{\pi\alpha}{2}\right)(2\pi f)^\alpha, \tag{2.12}$$

2.2 Elastography

For more than 20 years, several groups have contributed to the field of elasticity imaging. While there are a variety of available techniques, they all share the following basic elements: (i) A force is applied to the tissue, (ii) the local motion produced in the tissue is measured, and (iii) an elasticity parameter is estimated from the measurements. The different elastographic techniques can be classified by the type of information they provide (qualitative or quantitative), by the way the force is applied to the tissue (mechanical or acoustic radiation force), and by the modality used (US, MRI, or optical coherence tomography). In this thesis, we only focus on ultrasound based elasticity imaging modalities. Table 2.1 shows a

Table 2.1: Elastography Modalities

Technique	Type	Force applied	Parameter measured	Authors	First publication	Reference
Sonoelastography	Qualitative	Mechanical	Vibration Amplitud	Lerner *et al.*	1987	[13]
Compression or Strain Elastography	Qualitative	Mechanical	Strain	Ophir *et al.*	1991	[14]
SWE	Quantitative	Radiation Force	SWS	Sarvazyan *et al.*	1998	[15]
Vibroacoustography	Quantitative	Radiation Force	Local acoustic response	Fatemi *et al.*	1999	[16]
Transient Elastography	Quantitative	Mechanical	SWS	Catheline *et al.*	1999	[17]
ARFI	Qualitative	Radiation Force	Peak displacement	Nightingale *et al.*	1999	[18]
CWS	Quantitative	Mechanical	SWS	Wu *et al.*	2004	[19]
SSI	Quantitative	Radiation Force	SWS	Bercoff *et al.*	2004	[20]
Vibro Elastography (VE)	Qualitative	Mechanical	Induced tissue motion	Turgay *et al.*	2006	[21]
SMURF	Quantitative	Radiation Force	SWS	McAleavey *et al.*	2007	[22]
CUSE	Quantitative	Radiation Force	SWS	Song *et al.*	2012	[23]
STL-ARFI	Quantitative	Radiation Force	SWS	McAleavey *et al.*	2013	[24]

summary of these techniques.

2.2.1 Elasticity Imaging based on mechanical sources of vibration

2.2.1.1 Vibration amplitude sonoelastography

Lerner et al. proposed the idea of particle vibration displacement estimation using Doppler ultrasound [13]. Sonoelastography uses external mechanical sources to apply a low-frequency (20-1000 Hz) and low amplitude (20 to 100 μm) excitation to generate internal sinusoidal vibrations in the tissue under inspection. The low amplitude of excitation ensures a safe, non-invasive method and the low frequency reduces the shear wave attenuation to enable deeper penetration in the tissue. The motion is then detected by Doppler ultrasound using a simple relationship between the Doppler spectral variance and the sinusoidal vibration

amplitude of particles in the tissue. Although, the main clinical focus of sonoelastography has been prostate cancer detection [25, 26, 27, 28], it has also been used in liver [25, 29], breast [30, 31], kidney [25]. Vibration sonoelastography has shown better sensitivity and predictive values than B-mode imaging for in vitro results in prostate cancer [32]. The advantage of this technique is that it is compatible and easy to implement in commercially available US scanners. The main disadvantage is the need for an external vibration source which can introduce variability in the measurements. Figure 2.3 shows matching B-mode and sonoelastographic images of an in vivo human prostate. A cancerous tumor is shown in both images. The lack of vibration (represented by the void in the green background) in the sonoelastographic image is characteristic of a hard lesion adding to the diagnostic value of the B-mode image.

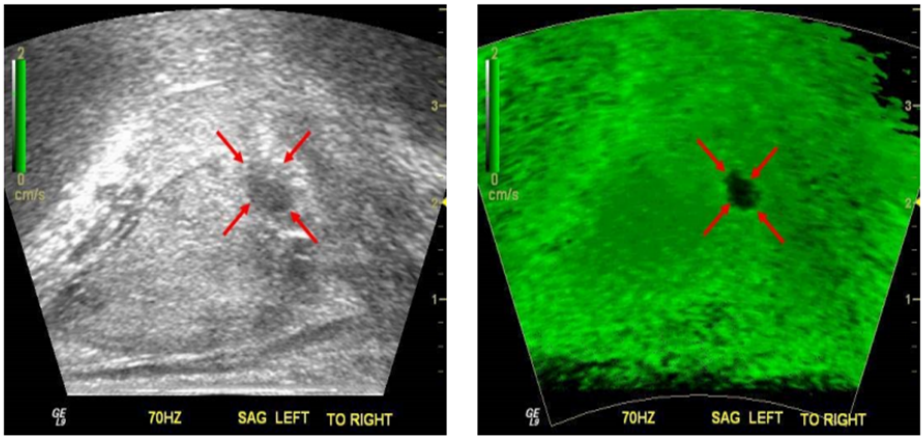

Figure 2.3: (left) B-mode US and (rigth) sonoelastographic images from an in vivo prostate study. The sonoelastographic image reveals a stiff (cancerous) mass (denoted by arrows) in the middle of the image [2].

2.2.1.2 Crawling Waves Sonoelastography

Crawling Wave Sonoelastography is an elasticity imaging technique proposed by Wu et al. [19]. In this technique, two opposing shear wave vibration sources are operated at slightly offset frequencies and produce a slowly moving interference pattern, termed Crawling Waves (CW), which is imaged in real time using vibration sonoelastography. The apparent velocity of CW is proportional to the underlying shear velocity of the tissue and can be used to estimate locally its elasticity modulus. This technique offers a quantitative estimation of the elastic properties of the tissue. In addition, the use of two vibration sources drives more mechanical energy into the tissue improving the Signal-to-Noise Ratio (SNR) [2]. Under the plane wave assumption and considering a homogenous sample, the shear waves introduced by the right (W_r) and left (W_l) vibration sources can be described as follows:

$$W_r = e^{-\alpha\left(x+\frac{D}{2}\right)} e^{-j\left(k_1\left(x+\frac{D}{2}\right)-\omega_1 t\right)}, \tag{2.13}$$

$$W_r = e^{-\alpha(\frac{D}{2}-x)}e^{-j(k_2(\frac{D}{2}-x)-\omega_2 t)}, \tag{2.14}$$

where α is related to the attenuation of the wave in the sample, D is the distance between the sources, k_1 and k_2 are the wave numbers and ω_1 and ω_2 are the frequencies of the vibration sources. In this particular case $\omega_1 = \omega, \omega_2 = \omega + \Delta\omega$ and $k_1 = k, k_2 = k + \Delta k$, where $\Delta x\omega$ is the difference in frequency between the vibration sources.

The resulting pattern is the superposition of the two waves. The squared signal envelope will result in:

$$|u(x,t)|^2 = (W_r + W_l)(W_r^* + W_l^*), \tag{2.15}$$

$$|u(x,t)|^2 = 2e^{-\alpha D}[\cosh(2\alpha x) + \cos(2kx + \Delta x + \Delta\omega t)], \tag{2.16}$$

The interference patterns described in equation (2.16) depend on a hyperbolic cosine and a cosine term. In the central region and under weak attenuation, the hyperbolic cosine term becomes approximately constant. Under such consideration, the spatial frequency of the interference patterns becomes $2k$. Thus, the interference fringe spacing is half the intrinsic shear wave wavelength (λ). The shear wave speed is estimated as:

$$c_s = \frac{\omega}{k}, \tag{2.17}$$

$$k = \frac{\theta'}{2}, \tag{2.18}$$

where θ is the phase of the cosine term. We obtained the phase by taking the Fourier transform of each pixel projection of the crawling wave image over the time axis.

The shear wave speed can be estimated in different ways. Local frequency estimators were proposed by Wu et al. [19]. McLaughlin et al. [33] presented a method in which features of the CW and arrival times at points in the image plane are used to calculate the local shear velocity distribution in the image. Hoyt et al. [34] proposed a real-time estimator based on autocorrelation methods. In order to obtain a relationship between shear wave speed and the elasticity modulus (E), it is assumed that soft tissues are nearly incompressible, and, therefore, their Poissons ratio (ν) is approximately 0.5. The shear modulus (G) can be related with the elasticity modulus by:

$$G = \frac{E}{2(1+\nu)} \approx \frac{E}{3} \tag{2.19}$$

Therefore, for a nearly incompressible biomaterial, a measurement of the shear wave speed can be related with elasticity modulus as:

$$c_s \approx \sqrt{\frac{E}{3\rho}} \tag{2.20}$$

We can use (2.20) to obtain information about the stiffness of the material. Crawling wave sonoelastography has been successfully applied to detect radio frequency ablated hepatic le-

sions in vitro [35], to characterize human skeletal muscle in vivo [36, 37] and to characterize human prostate tissue ex vivo [2].

In Figure 2.4, we can see a crawling wave image of a gelatin phantom with a central stiffer inclusion. The interference pattern shows a different shear wave speed inside the red circle (a longer wavelength of the interference pattern) due to the stiffer material. This image was taken at the Sonoelasticity Laboratory of the University of Rochester using a GE Logiq 9 (GE Healthcare, Wauwatosa, WI, USA) scanner.

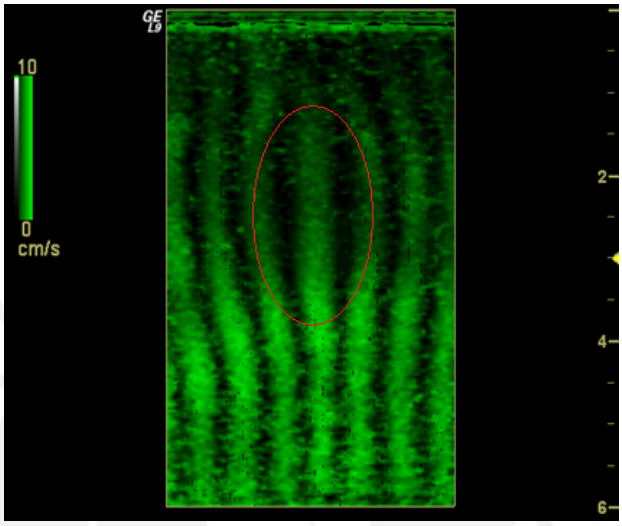

Figure 2.4: Crawling wave image of a gelatin phantom with a vibration frequency of 290 Hz and 0.35 Hz offset. The red circle shows an area of longer wavelength in the pattern and, therefore, of higher shear velocity.

2.2.2 Elasticity Imaging based on Acoustic Radiation Force

In addition to applying an external vibration or compression in the tissue, it is possible to create motion within tissue using acoustic radiation force (ARF). ARF is a phenomenon related to the attenuation of acoustic waves in a medium or tissue. Ultrasound waves transfer part of their momentum to the tissue and consequently push the local tissue from the inside and along the wave propagation direction [42]. In the case of soft tissue, absorption is the predominant attenuation mechanism in the medium. In this case, radiation force generated from an acoustic plane wave can be expressed as follows [18]

$$F = \frac{2\alpha I}{c}, \tag{2.21}$$

where F is the acoustic radiation force, α is the absorption coefficient of the tissue, I is the time-averaged acoustic beam intensity, and c is the speed of sound in the medium.

The spatial distribution of this radiation force is dependent on the focal configuration of the transducer, which is often characterized by the transducer f-number (F/#), and the spatial distribution absorption coefficient of the material. As seen in Table 2.1, there are different elastography techniques which use ARF. In the case of quantitative techniques based in

ARF, they estimate the shear wave speed (c_s) within the tissue.

2.2.2.1 Acoustic Radiation Force Impulse (ARFI)

Nightingale et al. [18] proposed this technique. ARFI imaging uses a series of high intensity pushing beams of short duration (0.03-0.4 ms) to generate localized displacements (between 1 and 20), and these displacements are tracked by ultrasound pulses of low pulse repetition frequencies (3 to 12 kHz) [43]. The response of the tissue to these forces is monitored to obtain images depicting the peak displacement or the time of recovery. The same US transducer is used to generate the ARF and to track the resulting displacements. Thus, ARFI does not require additional hardware. However, as a disadvantage, the repetitive use of ARF increases the temperature of the tissue. For this reason, the intensity and the duration of the push pulses are limited to avoid heating and cavitation [43]. Figure 4.12 show an ARFI image example of an inhomegeneous phantom.

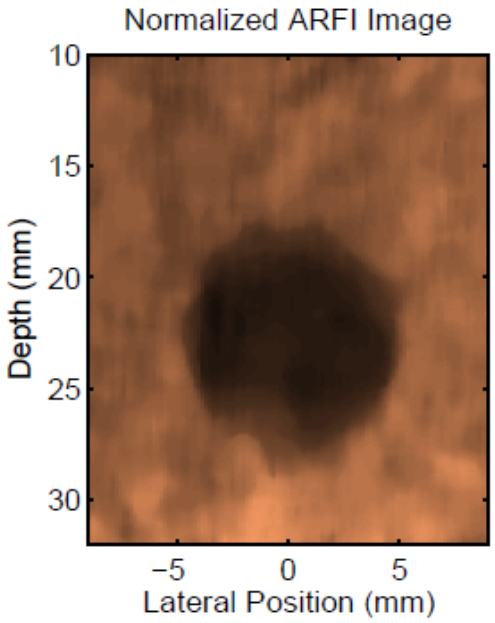

Figure 2.5: Normalize ARFI images of a 10.4 mm cylindrical inclusion in a soft background [4]

2.2.2.2 Single Tracking Location-ARFI

STL-ARFI is an elastographic modality proposed by McAleavey [24] based on ARF that involve tracking in a single location, as opposed to multiple locations like others techniques based on ARF (for example: ARFI, SSI, SWE). The disadvantage in ARF modalities that applies multiple tracking is they are more sensitive to speckle-induced bias in phase estimation, due to the fact that stronger speckle are tracked preferentially, and they may be located off the axis of the tracking beam. In the other hand, STL-ARFI track at one location and avoids this source of error improving the shear wave speed estimation. In the

STL-ARFI algorithm, the ARF is applied at two locations, $P1$ and $P2$, and the induced shear waves is tracked at one location, T. Figure 2.6 shows the STL-ARFI algorithm representation. The shear modulus estimate is associated with the region between $P1$ and $P2$. The displacements are estimated using normalized cross-correlation on the reference and post-push echoes. The finite-time difference of the slow-time displacement is calculated to get the velocity data. The velocity data, associated with the two pushes, is cross-correlated to extract the arrival time difference between both waves. After that, the shear wave speed can be estimated using (2.19) and (2.20). This technique has been applied in phantoms and excised porcine liver tissue [44, 24].

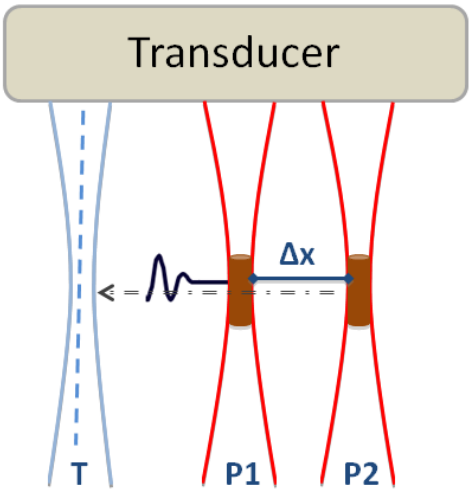

Figure 2.6: STL-ARFI representation. First push pulse ($P1$) is applied and tracked in T. Then, $P2$ is applied and tracked at position T again.

The shear wave speed can be estimated using equation (2.22):

$$c_s = \frac{\Delta x}{\Delta t}, \tag{2.22}$$

where Δx is the distance between $P1$ and $P2$, and Δt is the arrival time difference.
In order to have a relationship between the SWS and frequency using STL-ARFI and thus, make a comparison with CWS results, a analogous methodology applied by Langdon et al. [45] was implemented. To achieve this result, the knowledge of the tracked velocity signal s_1 and s_2 generated by the two ARF pushes (s_2 apart of s_1 by a Δx distance) was used.Then, the Fourier Transform of s_1 and s_2 were obtained, both Fourier transforms can be model as [45]:

$$S_1(f) = A_o e^{j(\phi+(x_o+x_{e1})k(f))}, \tag{2.23}$$

$$S_2(f) = \beta A_o e^{j(\phi+(x_o+x_{e1}+\Delta x)k(f))}, \tag{2.24}$$

Here S_1 and S_2 are the Fourier transform of s_1 and s_2, respectively, A_o is the amplitude of the original excitation with phase ϕ, β is some proportionality constant, k is the wavenumber,

x_{e1} and x_{e2} are the uncertainty in the tracking location due to speckle bias. When a single track location is used, $x_{e1} = x_{e2}$.

Taking the expectation value for the ratio of all S_2 to S_1 generated in a region of interest yields:

$$\langle P(f) \rangle = \frac{S_2}{S_1} = \beta e^{j(\Delta x)k(f)}, \tag{2.25}$$

By talking the phase of $\langle P(f) \rangle$, the wavenumber k can be obtained using:

$$k(f) = \frac{\angle\{\langle P(f) \rangle\}}{\Delta x}, \tag{2.26}$$

Then, equation 2.17 can be used to obtain the SWS for a frequency range corresponding to S_1 and S_2.

Chapter 3

Materials and Methods

In this section we describe the experiments using homogeneous and inhomogeneous phantoms. All the experiments were performed at room temperature (16^{o}C-17^{o}C) and on the same day to avoid changes in the phantom materials. The mechanical testing and ultrasound scans were made in three different laboratories at the University of Rochester.

3.1 Gelatin phantoms

3.1.1 Homogeneous phantoms

Homogeneous elastic phantoms were constructed following the procedure used by Hah et al. [46]. Three different phantoms with gelatin (300 Bloom Pork Gelatin, Gelatin Innovations Inc.) concentrations of 10%, 13% and 16% were created by heating a mixture of gelatin, 1.8 l of degassed water, 16.2 g of Na-Cl, 36 g of graphite and 2.7 g of agar to 50^{o}C. The mixture was then cooled to approximately 30^{o}C and poured into a cubic mold. The mold was then allowed to rest at 4^{o}C overnight. Figure 4.10 shows a 10% gel phantom used in the experiments.

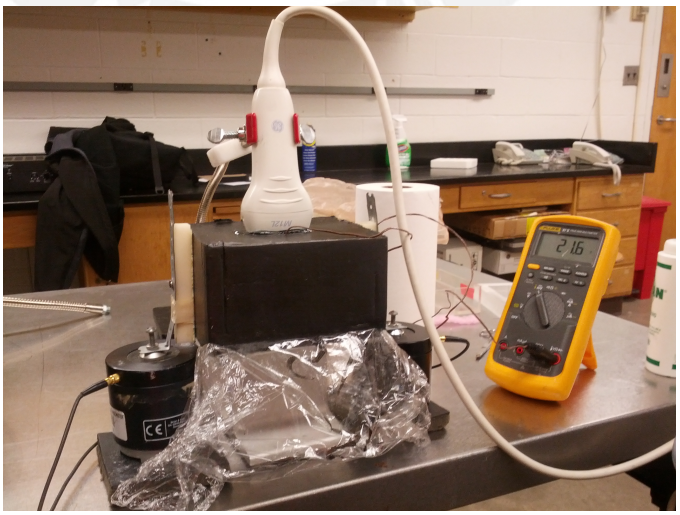

Figure 3.1: Homogeneous 10% gel phantom in a CWS experiment. The phantom was made using the procedure explained previously

3.1.2 Inhomogeneous phantoms

Two different inhomogeneous phantoms were created. The first one consisted on a two layer phantom (one region softer than the other). The second phantom consisted of a conical inclusion embedded in an otherwise homogeneous background (cone phantom). This inclusion geometry allowed to construct elastographic images where the cross-section of the inclusion consisted of circles with smoothly varying diameters ranging from 0 cm up to 1.8 cm. For both types of phantoms, the two different regions were constructed using the same procedure described above for the homogeneous phantoms using gelatin concentrations of 13% and 10%, inclusion and background media for the cone phantom, respectively. The cone phantom shape and the transducer position for scanning purposes are shown in Fig. 3.2.

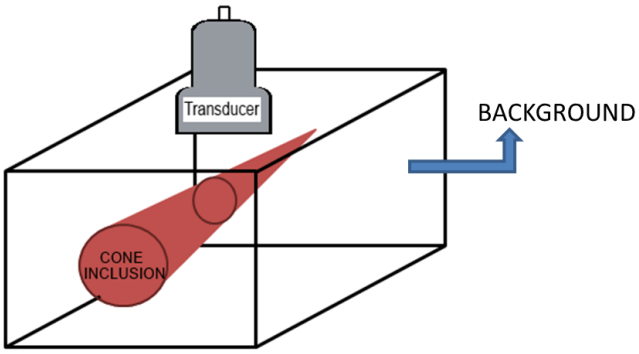

Figure 3.2: Inhomogeneous phantom diagram. The inclusion is stiffer than the background and its conical shape allows imaging cross-sections with structures of varying diameters.

3.2 Shear Wave Speed estimation using Mechanical Measurements

For each physical phantom, stress relaxation tests were performed on three cylindrical samples (approximately 38 mm in diameter and 33 mm in length) made with the same mixture used to construct the gelatin-based media. The mechanical tests were applied using the procedure described by Zhang et al. [1]. A QT/5 mechanical device (MTS Systems Co., Eden Prairie, MN, USA) with a 5 N load cell was used to test the samples (See Fig. 4.9). The upper and lower plates were coated with vegetable oil before testing. The samples were put on the center of the lower testing plate. The top plate was used as a compressor and carefully positioned to fully compress the sample. The compression rate and the strain value were adjusted to 0.5mm/s and 5%, respectively. The tests lasted about 700s. The resulting data consisted of a plot of stress versus time. The stress relaxation curve of each sample was fitted to the Kelvin Voigt Fractional Derivative (KVFD) model using the MATLAB® Curve Fitting Toolbox (The Mathworks, Inc., Natick, MA, USA). The trust-region method

for nonlinear least squares fitting was applied to each curve. The averaged three model parameters, E_o, η and α, were then obtained. These model parameters were then used in (2.11) to estimate the elasticity modulus at any frequency.

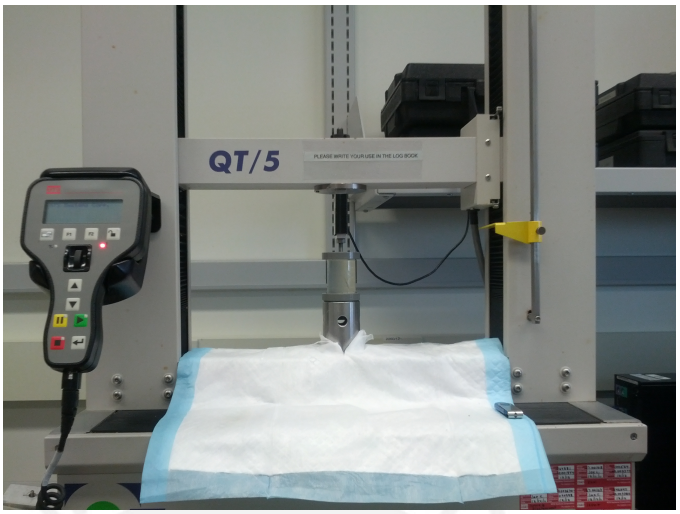

Figure 3.3: Mechanical measurement experiment using a QT/5 mechanical device

3.3 Shear Wave Speed estimation using Crawling Waves Sonoelastography

An amplifier (model 5530, AE Techron, Elkhart, IN, USA) driven by a dual channel function generator (model AFG3022B, Tektronix, Beaverton, OR, USA) provided input signals to two mechanical vibration sources (model 4810, Brüel & Kjaer, Naerum, Denmark), vibrating at low frequency (160-500 Hz) and placed opposite each other. These were applied to phantoms to generate a relatively uniform vibration field. A GE Logiq 9 ultrasound system (GE Healthcare, Wauwatosa, WI, USA) was used to perform sonoelastographic imaging and a linear array ultrasound transducer (M12L, GE Healthcare, Wauwatosa, WI, USA) was positioned between the vibration sources. Figure 3.4 describes the setup for the crawling waves sonoelastography technique.

3.4 Shear Wave Speed estimation using Single Tracking Location-ARFI

A Siemens Antares scanner (Siemens Medical Solutions, USA) and a linear array transducer, a Siemens Antares VF7-3 linear array, were used to generate pushing beams as well as to track the induced displacements. The center frequency of both the push and track pulses was 4.21 MHz. In the STL-ARFI algorithm, the acoustic radiation force was applied at two locations, $P1$ and $P2$, and the induced shear waves were tracked at one location, T, 5.32 mm from $P1$. The distance between the pushing pulses, Δx, was varied between 2.66 mm and 6.20 mm, to evaluate how Δx influences the lateral resolution, contrast and CNR

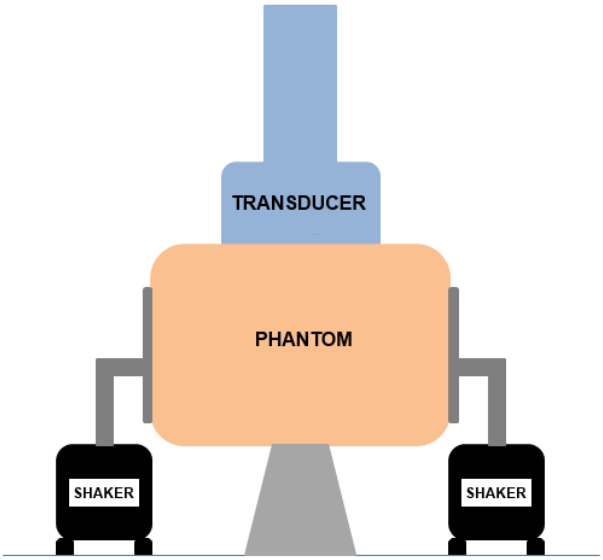

Figure 3.4: Experimental setup for CWS. Both mechanical vibration sources are placed opposite each other in order to generate the crawling waves

estimation. The post-push tracking echoes were received at a pulse repetition frequency of 7.5 kHz. Then, normalized magnitude spectrum was used to estimate the frequency range of the velocity signal generated by the acoustic radiation force at $P1$ and $P2$.
All the images that shows the SWS results obtained using STL-ARFI are presented using equation (2.22). In addition, equation (2.26) and (2.17) were implemented in order to have a relationship between SWS and frequency. In order to know the frequency range, the velocity signals spectra bandwidth using the -3dB point criterion was estimated. Therefore, a comparison between the SWS values obtained using CWS and STL-ARFI can be presented for a range of frequencies and validated with MM.

3.5 Lateral Resolution Estimation

In the inhomogeneous phantoms, the SWS profiles across the cone inclusion were fit into a double sigmoid function [see (3.1)] to estimate the spatial resolution [47], i.e.

$$c(x) = (c_{in} + c_{out})\left(\frac{1}{1+e^{\frac{x_1-x}{\lambda_1}}}\right)\left(\frac{1}{1+e^{\frac{x-x_2}{\lambda_2}}}\right) + c_{out}, \tag{3.1}$$

where x is the lateral position, c_{in} and c_{out} are the SWS in the inclusion and background, x_1 and x_2 are the locations of the inclusion boundaries, and λ_1 and λ_2 represent the widths of the transition from the background into the inclusion, and from the inclusion into the background, respectively.
For the two layer phantom, (3.1) can be simplified to:

$$c(x) = (c_{in} + c_{out})\left(\frac{1}{1 + e^{\frac{x_1 - x}{\lambda_1}}}\right) + c_{out}, \tag{3.2}$$

where c_{in} and c_{out} are the SWS in the stiffer and softer regions. The other parameters represents the same properties as eq.(3.1)

The estimation of λ_1 and λ_2 allow the SWS resolution R_{2080}, defined as the distance required for a 20% - 80% transition of the SWS [47], to be evaluated quantitatively as:

$$R_{2080,i} = 2ln(4)\lambda_i, \tag{3.3}$$

for the two layer phantom, $i = 1$.

3.6 Contrast and CNR Estimation

The contrast and CNR were evaluated in the SWS images from the inhomogeneous phantoms using (3.4) and (3.5):

$$contrast = \frac{|\mu_{in} - \mu_{out}|}{\mu_{out}}, \tag{3.4}$$

$$CNR = \frac{|\mu_{in} - \mu_{out}|}{\sqrt{\sigma_{in}^2 + \sigma_{out}^2}}, \tag{3.5}$$

where μ_{in} and μ_{out} are the mean values of the SWS at rectangular regions within the inclusion and background regions, respectively, and σ_{in} and σ_{out} are the standard deviation of the same regions respectively.

Chapter 4

Experimental Results

4.1 Mechanical Measurements

Figure 4.1 shows a typical stress relaxation curve of a sample and its fit using the KVFD model for the gelatin based phantoms (10%, 13% and 16%). For all the measurements, each curve fitting had a correlation coefficient value larger than 0.965, demonstrating that the use of the KVFD model was appropriate for this study.

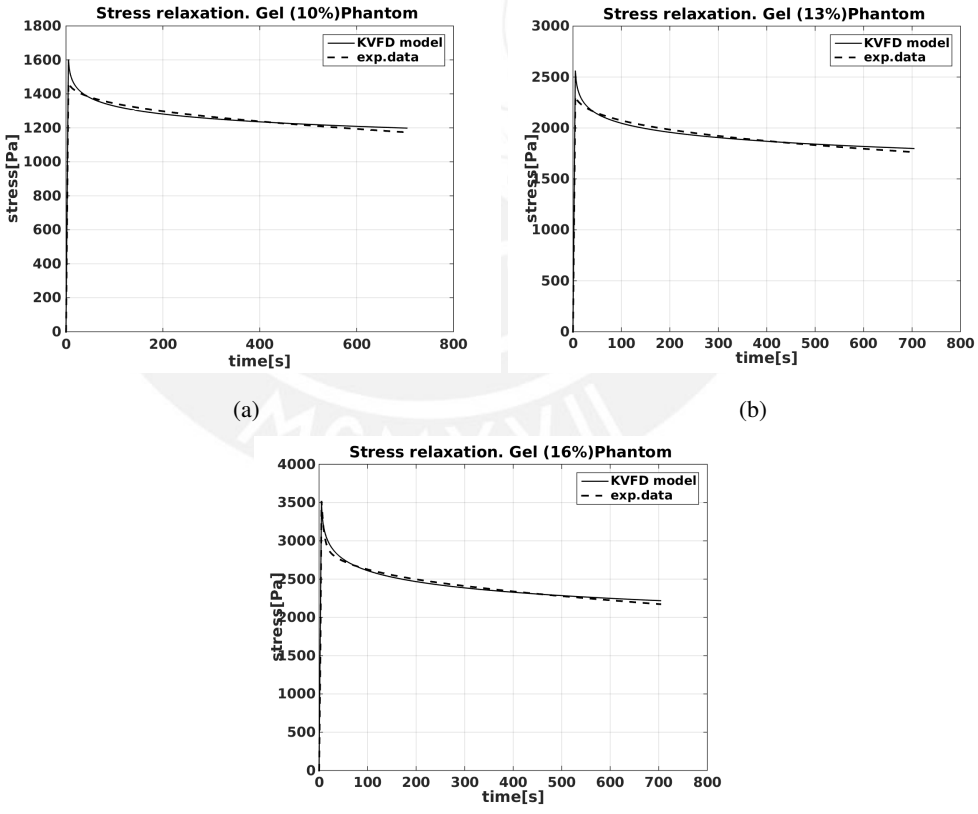

(a) (b)

(c)

Figure 4.1: Stress relaxation curve from: (a) 10% gelatin phantom, (b) 13% gelatin phantom and (c) 16% gelatin phantom. All of them with their fitting using the KVFD model

4.2 Frequency Range Estimation from STL-ARFI

The spectrum magnitude of the velocity signal from STL-ARFI was estimated by taking its Fourier transform in order to obtain its frequency range. For all the experiments, using the criteria explained in Chapter III, it was found that the frequency bandwidth ranges approximately from 140 to 1200 Hz. Figure 4.2 shows two velocity signals generated by $P1$ and $P2$ Fig.4.2.a and their corresponding spectrum Fig.4.2.b. The relationship between SWS and its corresponding frequency range using STL-ARFI can be illustrated in figure 4.4.

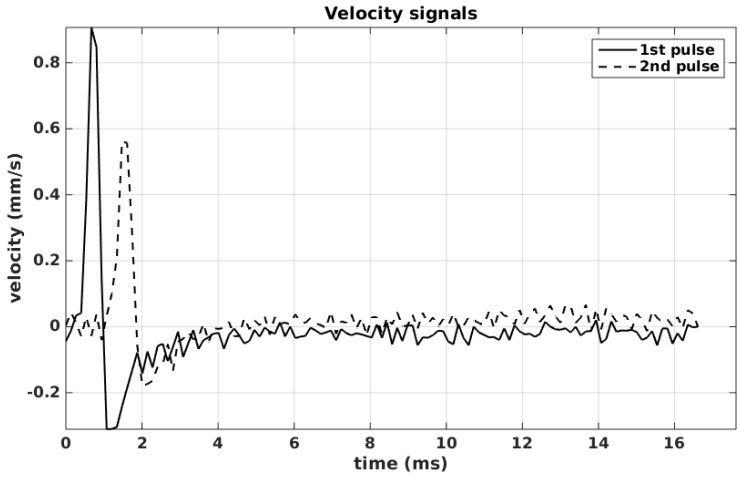

(a)

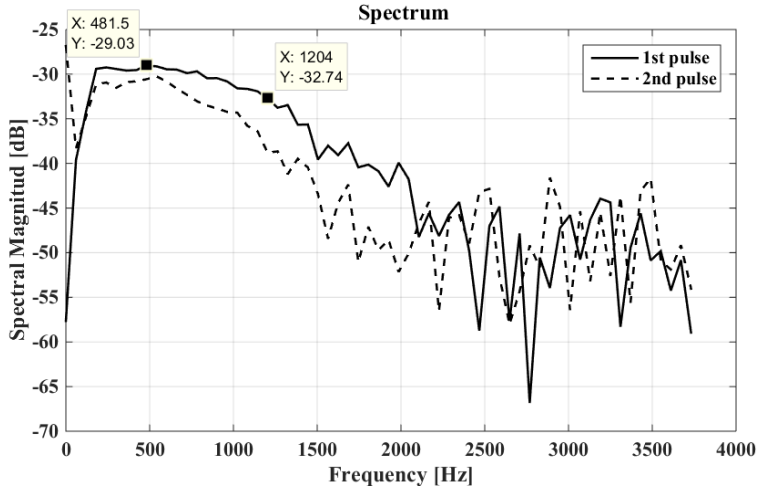

(b)

Figure 4.2: (a) Velocity signals generated by $P1$. and $P2$ (b) shows the spectrum of the velocity signals generated by $P1$ (solid line) and $P2$ (dash line). The square indicators illustrated the -3dB point criterion used in order to find the range frequency.

4.3 Shear Wave Speed estimation in Homogeneous Phantoms

Figure 4.3, shows shear waves images estimated with CWS (left images) and STL-ARFI (right images) for a 10% gelatin phantom [Fig.4.3.a and Fig.4.3.b], 13% [Fig.4.3.c and

Fig.4.3.d] and 16% [Fig.4.3.e and Fig.4.3.f]. For all cases, a CWS image estimated using a 380 Hz vibration frequency (Vf) and a STL-ARFI image using Δx equal to 4.43 mm are displayed for comparison purposes. Subsequently, a region of interest (1.5 x 1.0 cm) was extracted from the center of each image to obtain the shear wave speed average and its standard deviation.

Figure 4.4 shows the comparison plots of the shear wave speed as a function of frequency using CWS, STL-ARFI, and MM in the region of interest for all phantoms. In CWS, a good agreement was obtained in comparison with MM for all the different phantoms. Table 4.1 and 4.2 present the SWS values estimated with CWS and MM and the accuracy errors respect to MM, respectively, for some of the vibration frequencies used in this work. The maximum accuracy errors obtained were 2.52%, 1.63% and 2.26% for the 10%,13% and 16% gelatin phantom at 160 Hz respectively. In STL-ARFI, better agreement compared with MM was obtained at a higher frequency range than the used for CWS. Table 4.3 and 4.4 presents the SWS values estimated with STL-ARFI and MM and the accuracy errors respect to MM, respectively, for some values of the estimated operating frequency range. The maximum accuracy errors obtained were 6.22%@240Hz, 5.63%@180Hz and 4.08%@180Hz for the 10%,13% and 16% gelatin phantom respectively. Consequently, it can be seen that CWS has a better performance in the estimation of SWS in lower frequencies and STL-ARFI has better performance for higher frequencies. It can be noted that since the phantoms are almost pure elastic material the dispersion results (relationship between SWS-Frequency) remains almost constant in the whole frequency range.

Table 4.1: SWS estimation at different frequencies using CWS compared with MM $[m/s]$

Type of phantom	Modality	160 Hz	220 Hz	280 Hz	340 Hz	400 Hz	460 Hz	500 Hz
10% Gel	CWS	4.11	4.03	4.02	4.08	4.07	4.09	4.10
	MM	4.02	4.04	4.06	4.07	4.09	4.10	4.10
13% Gel	CWS	5.13	5.11	5.10	5.15	5.16	5.20	5.15
	MM	5.04	5.08	5.10	5.12	5.14	5.16	5.17
16% Gel	CWS	6.00	5.92	6.02	5.98	6.02	6.05	6.04
	MM	5.87	5.92	5.95	5.98	6.00	6.02	6.03

Table 4.2: SWS error with respect to MM using CWS [%]

Type of phantom	160 Hz	220 Hz	280 Hz	340 Hz	400 Hz	460 Hz	500 Hz
10% Gel	2.52	0.07	0.63	0.38	0.10	0.10	0.08
13% Gel	1.63	0.71	0.07	0.48	0.33	0.81	0.27
16% Gel	2.26	0.05	1.16	0.13	0.40	0.47	0.10

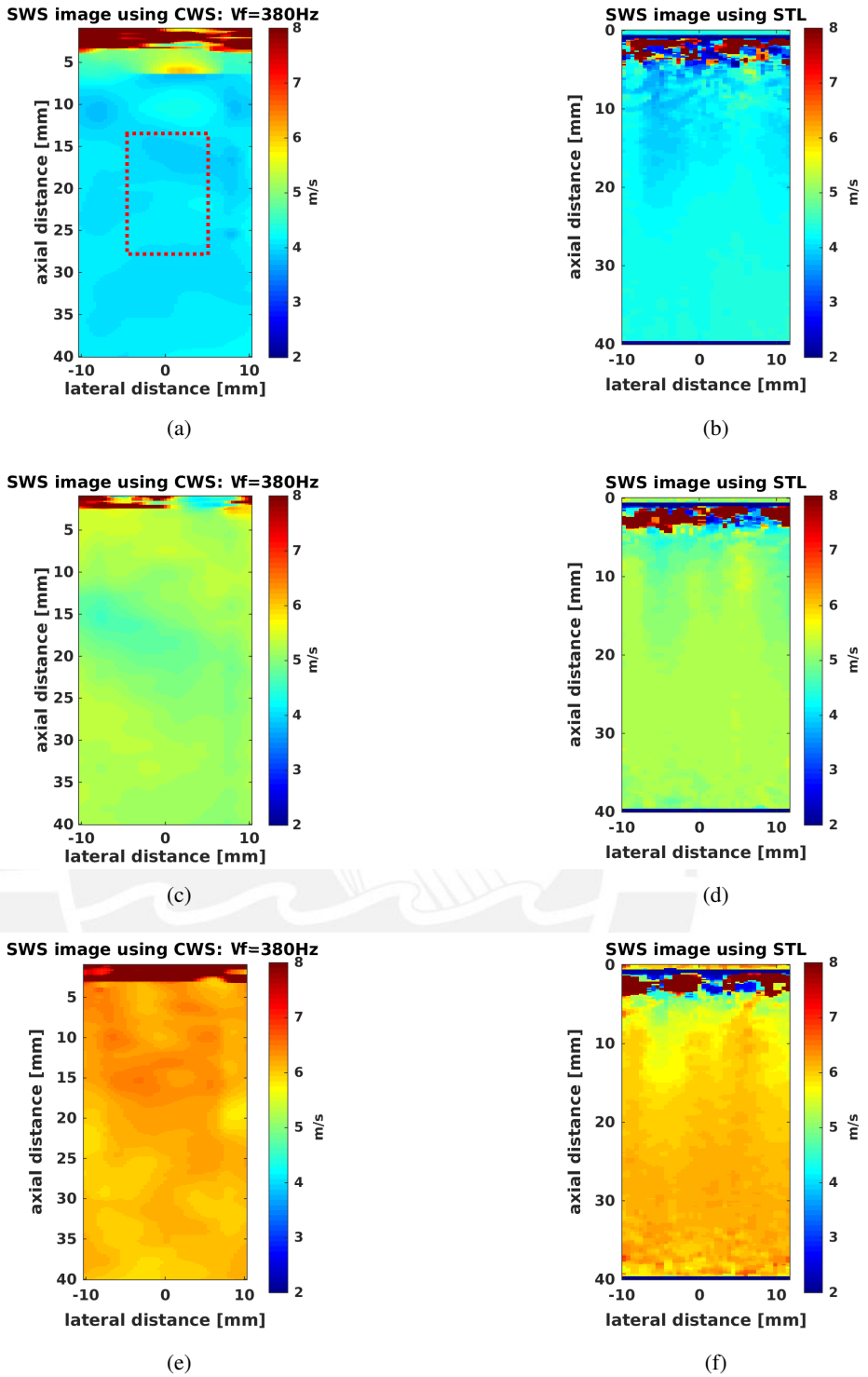

Figure 4.3: Shear wave speed maps estimated with CWS (left column) and STL-ARFI (right column) for a 10%, 13% and 16% gelatin phantom. The CWS images correspond to 380 Hz vibration frequency and Δx equal to 4.43 mm. The red square line in (a) illustrated the region of interest extracted for all images

4.4 Shear Wave Speed estimation in Inhomogeneous Phantoms

The SWS images estimated by CWS for the two layer and cone phantom are presented in Fig.4.5 and Fig.4.7 respectively. Similarly, Fig.4.6 and Fig.4.8 shows the SWS images es-

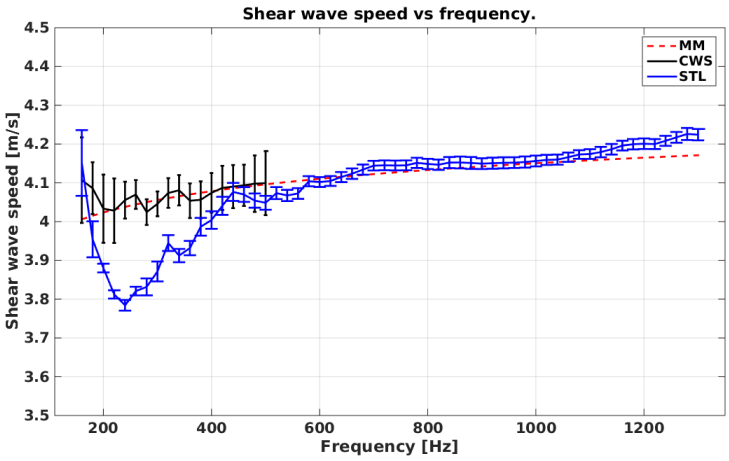

(a)

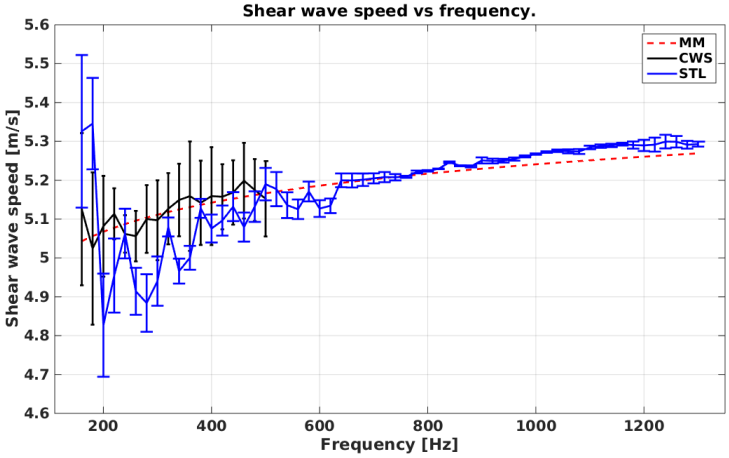

(b)

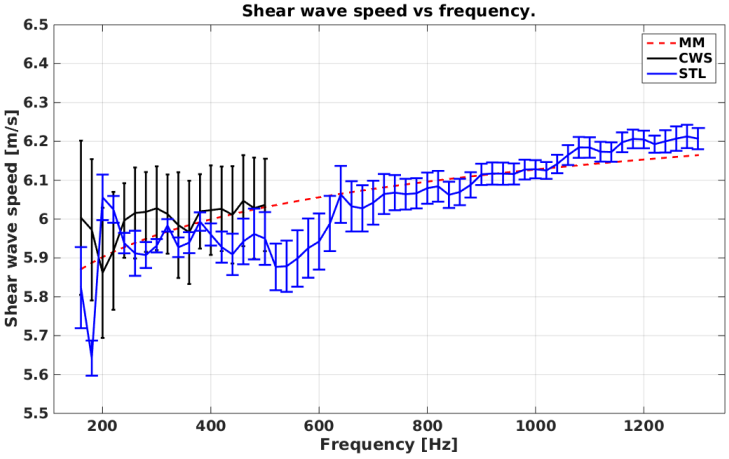

(c)

Figure 4.4: Comparison plots of CWS, STL-ARFI, MM using the KFVD model for a 10% gelatin phantom. (Fig.4.3.a), 13% (Fig.4.4.b) and 16% (Fig.4.4.c)

timated by STL-ARFI for the two layer and cone phantom, respectively. It is worth noting that Fig.4.5, Fig.4.7 and Fig.4.6, Fig.4.8 do not correspond exactly to the same scanning position because the CWS and STL-ARFI images were derived from different datasets ob-

Table 4.3: SWS estimation at different frequencies using STL-ARFI compared with MM $[m/s]$

Type of phantom	Modality	160 Hz	340 Hz	500 Hz	680 Hz	860 Hz	1020 Hz	1200 Hz
10% Gel	STL	4.15	3.91	4.05	4.13	4.15	4.16	4.20
	MM	4.02	4.07	4.10	4.12	4.14	4.15	4.16
13% Gel	STL	5.33	4.97	5.19	5.20	5.24	5.27	5.29
	MM	5.04	5.12	5.17	5.20	5.22	5.24	5.26
16% Gel	STL	5.82	5.93	5.95	6.03	6.07	6.13	6.20
	MM	5.87	5.98	6.03	6.07	6.11	6.13	6.15

Table 4.4: SWS error respect to MM using STL-ARFI [%]

Type of phantom	160 Hz	340 Hz	500 Hz	680 Hz	860 Hz	1020 Hz	1200 Hz
10% Gel	3.56	3.76	1.16	0.34	0.34	0.17	0.88
13% Gel	5.49	3.08	0.46	0.03	0.24	0.57	0.56
16% Gel	0.79	0.82	1.34	0.77	0.61	0.09	0.86

tained with different scanners. Fig.4.5 and Fig.4.7 shows the SWS images using different vibration frequencies. Fig.4.6 and Fig.4.8 presents the SWS images using STL-ARFI for different Δx values (3.54 mm, 5.31 mm and 6.2 mm).

4.5 Lateral Resolution Results

The lateral resolution was evaluated using the criteria described in Chapter 3. For both cases (CWS and STL-ARFI), good agreement was obtained when fitting the SWS profile across a region of interest for both type of inhomogeneous phantoms with the sigmoid or double sigmoid functions (i.e., correlation coefficients larger than 0.97 for all cases). Using equation (3.3) we obtained one or two R_{2080} values for the two layer and cone phantom, respectively. For all cases, the average between $R_{2080,1}$ and $R_{2080,2}$ were obtained. Fig.4.9.a and Fig.4.9.b shows the average SWS profile for the region of interest for Fig.4.5.c and Fig.4.5.d respectively and its corresponding fitting. Similarly, Fig.4.10.a and Fig.4.10.b shows the SWS profile for Fig.4.6.b and Fig. 4.6.d and its corresponding fitting.

The lateral resolution results versus frequency for the CWS experiments is shown in Fig. 4.11.a. It was found that the lateral resolution ranged between 4.19±0.52 mm and 2.38±0.51 mm for a frequency range from 220 Hz to 500 Hz. The frequency range used for the resolution estimation was equal to the one we used for homogeneous phantoms. However, lateral resolution estimation using vibration frequencies lower than 220 Hz were not good as we expected. This could be because with lower frequencies we have longer interference fringe spacing, thus, difficulty in differentiating targets increases. The lateral resolution

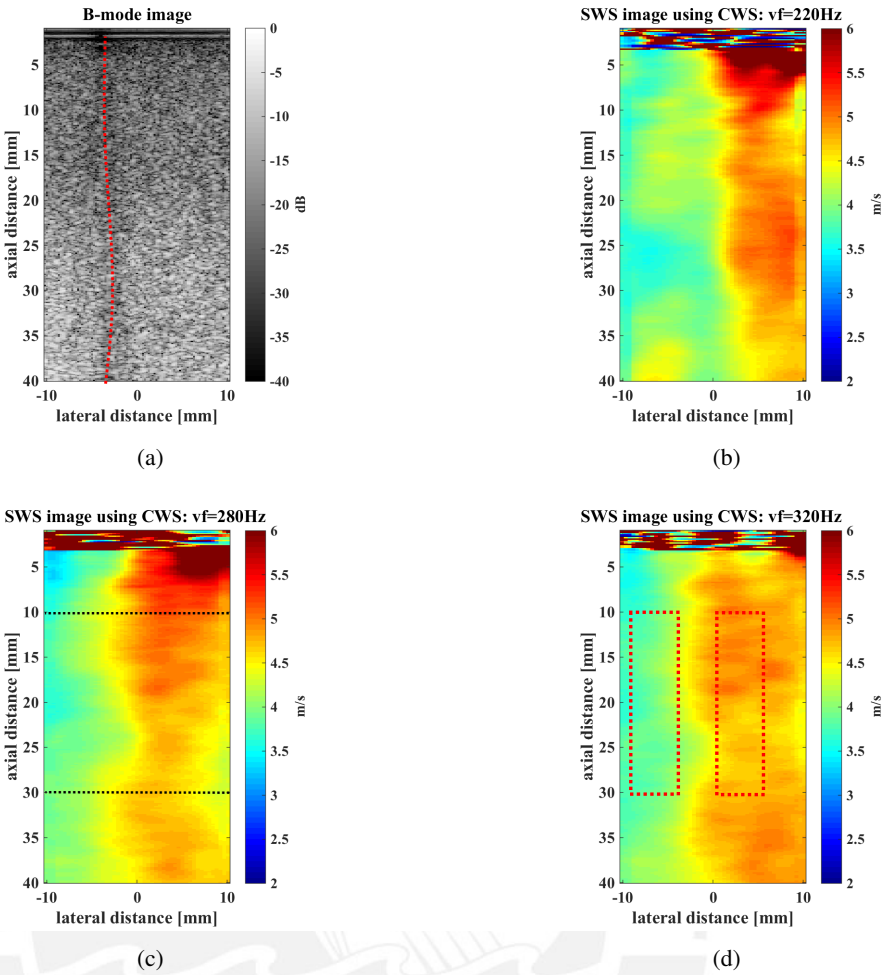

Figure 4.5: (a) Bmode image corresponding to the two layer phantom. The red dotted line indicates the boundary between the softer and stiffer region. (b-d) SWS images for inhomogeneous phantoms obtained with CWS for 220 Hz, 280 Hz and 320 Hz respectively. The black dotted lines in (c) indicates the region taken to obtain the average SWS profile. The red dotted rectangles in (d) shows the regions used to estimate the contrast and CNR.

versus Δx derived from the STL-ARFI images is shown in Fig.4.11.b. It was found that the lateral resolution estimation was equal to 2.45±0.75 mm-4.15±0.73 mm. This resolution range is comparable to the one obtained with CWS. As it can be seen, as the vibration frequency increases or Δx decreases, better lateral resolution could be obtained for CWS and STL-ARFI, respectively. This reasoning was expected for both type of modalities.

4.6 Contrast and CNR Results

For contrast and CNR estimation, we selected two different regions of the same size: [2x0.5] cm for the two layer phantom and [0.5x0.5]cm for the cone phantom. The contrast for both elastographic techniques is reported in Figs.4.12.a-4.12.b. Contrast values for CWS were in the range of 0.13±0.03 to 0.23±0.013, and in the case of STL-ARFI the contrast was in the range of 0.19±0.019 to 0.22±0.020. Fig.4.12.a shows that as the vibration frequency increases, the contrast tends to 0.25. Fig.4.12.b shows that contrast values estimated with

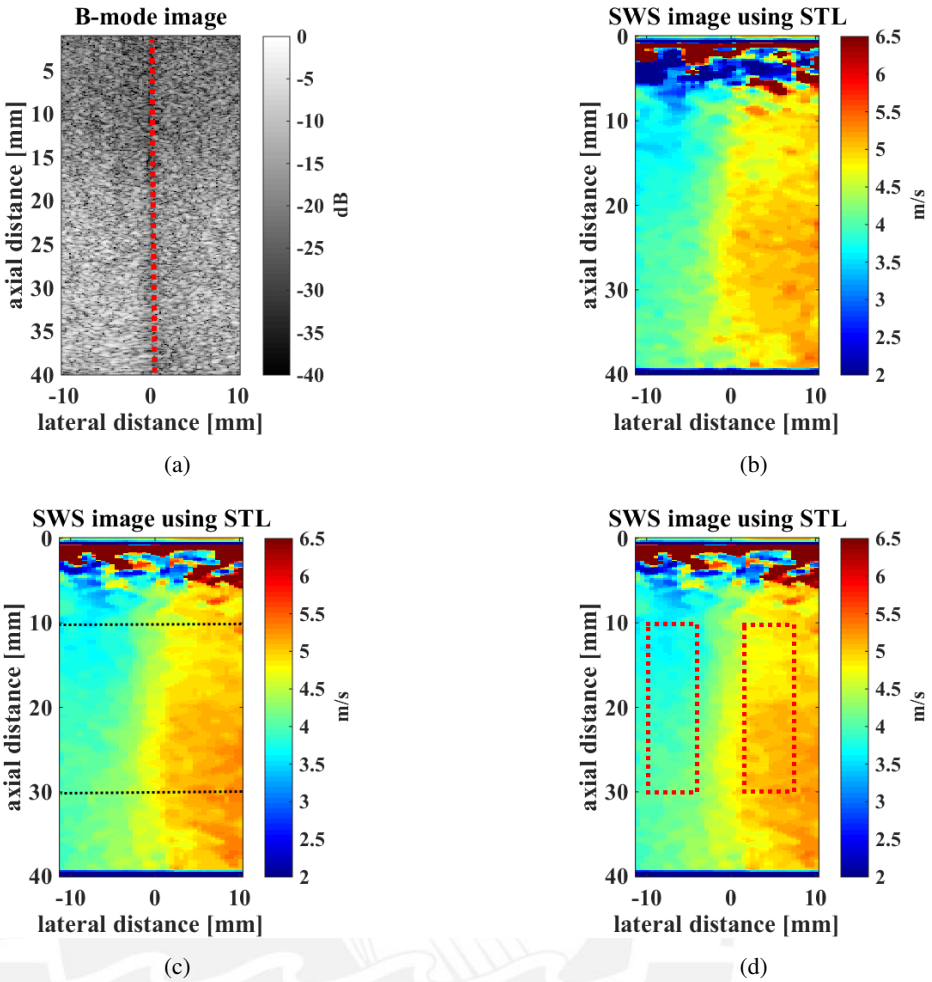

Figure 4.6: (a) Bmode image corresponding to the two layer phantom. The red dotted line indicates the boundary between the softer and stiffer region. (b-d) SWS images for inhomogeneous phantoms obtained with STL-ARFI for Δx equal to 3.54 mm, 5.31 mm and 6.2 mm respectively.The black dotted lines in (c) indicates the region taken to obtain the average SWS profile. The red dotted rectangles in (d) shows the regions used to estimate the contrast and CNR.

STL-ARFI tends to decrease as Δx increases. This result may be explained since the estimated SWS is an average of the region between the push beams. The CNR obtained with both techniques is shown in Figs.4.13.a-4.13.b. In this case, the CNR ranges between 3.01±0.29 and 6.04±0.33 for CWS and 3.88±0.98 and 6.09±0.58 for STL-ARFI. In the last case [see Fig.4.13.b], the CNR results presents higher standard deviations values compared with CWS-CNR results. Finally, Table 4.5 and 4.6 show the lateral resolution, contrast and CNR for some frequencies in CWS and for different Δx using STL-ARFI respectively.

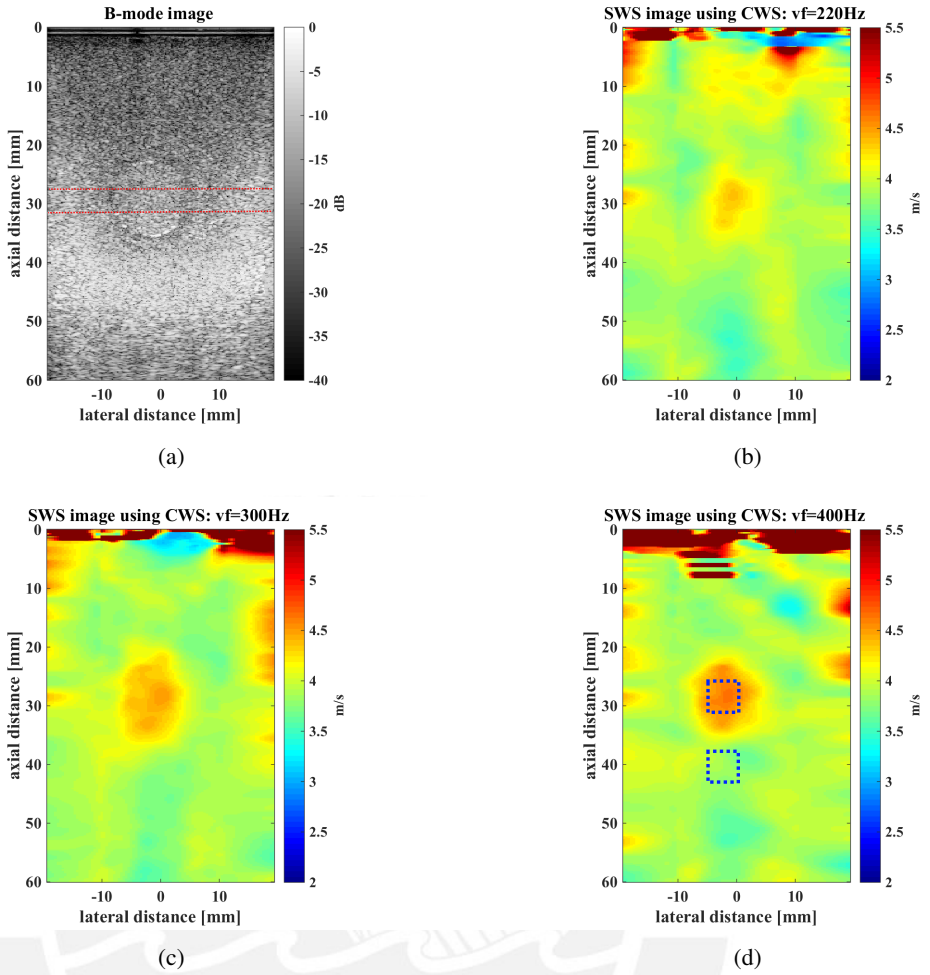

Figure 4.7: (a) Bmode image corresponding to the cone phantom. The black dotted lines in (a) illustrated the region taken to obtain the average SWS profile.(b-d) SWS images for cone phantoms obtained with CWS for 220 Hz, 300 Hz and 400 Hz respectively. The blue dotted squares in (d) shows the regions used to estimate the contrast and CNR.

Table 4.5: Lateral resolution, contrast and CNR for CWS

F_v [Hz]	240	280	340	400	460	500
Resolution [mm]	3.28	2.70	2.38	2.96	2.74	2.42
Contrast	0.13	0.18	0.23	0.22	0.22	0.24
CNR	3.55	4.57	5.57	5.94	5.79	6.04

Table 4.6: Lateral resolution, contrast and CNR for STL-ARFI

Δx [mm]	2.66	3.54	4.43	5.31	6.20
Resolution [mm]	2.45	2.95	3.34	3.53	4.15
Contrast	0.22	0.21	0.20	0.19	0.19
CNR	3.89	4.28	5.05	5.25	6.10

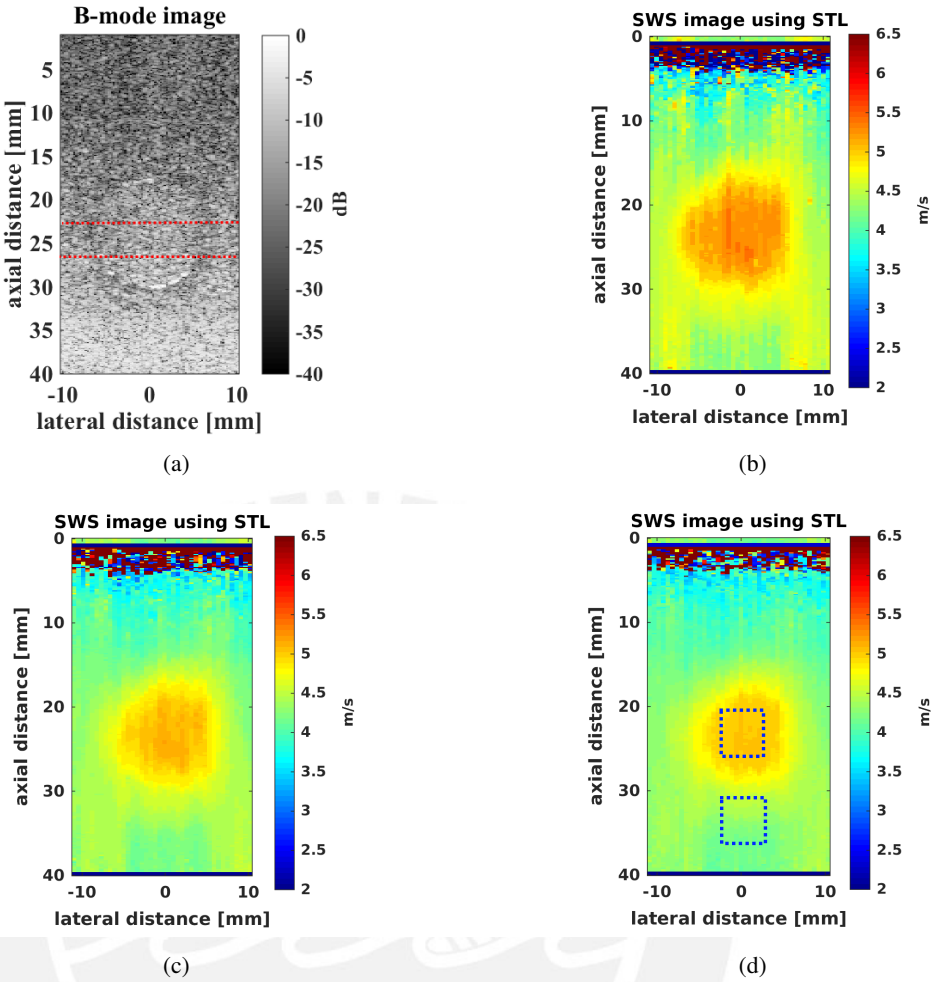

Figure 4.8: (a) Bmode image corresponding to the cone phantom.The black dotted lines in (a) illustrated the region taken to obtain the average SWS profile. (b-d) SWS images for inhomogeneous phantoms obtained with STL-ARFI for Δx values equal to 3.54 mm, 5.31 mm and 6.2 mm respectively. The blue dotted squares in (d) shows the regions used to estimate the contrast and CNR.

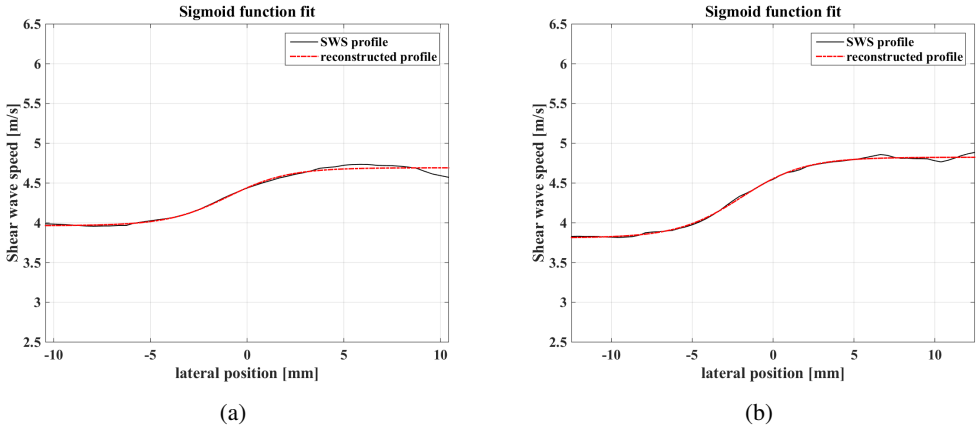

Figure 4.9: SWS profile and its reconstruction using a sigmoid function (dotted lines) in CWS using: (a) 280 Hz, (b) 320 Hz vibration frequency.

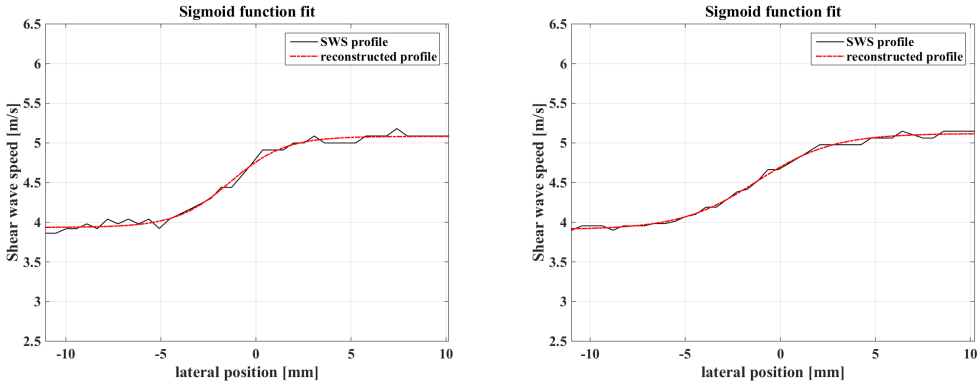

(a) (b)

Figure 4.10: SWS profile and its reconstruction using a sigmoid function (dotted lines) in STL-ARFI using Δx (a) 3.45 mm and (b) 6.2 mm.

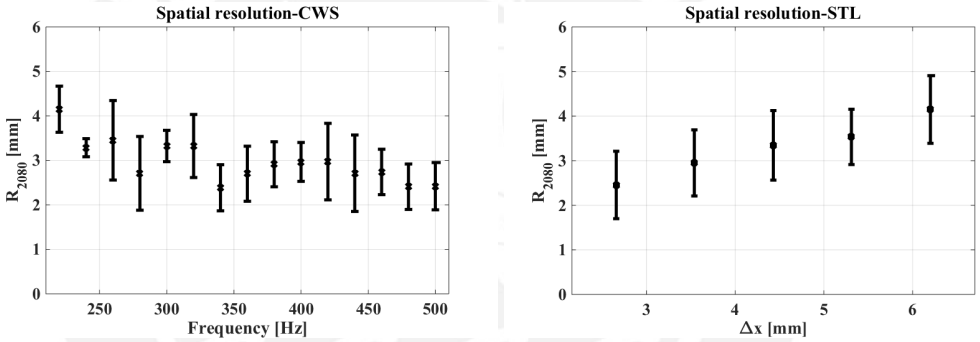

(a) (b)

Figure 4.11: Lateral resolution estimation. (a) shows lateral resolution vs frequency using CWS. (b) shows lateral resolution vs Δx using STL-ARFI.

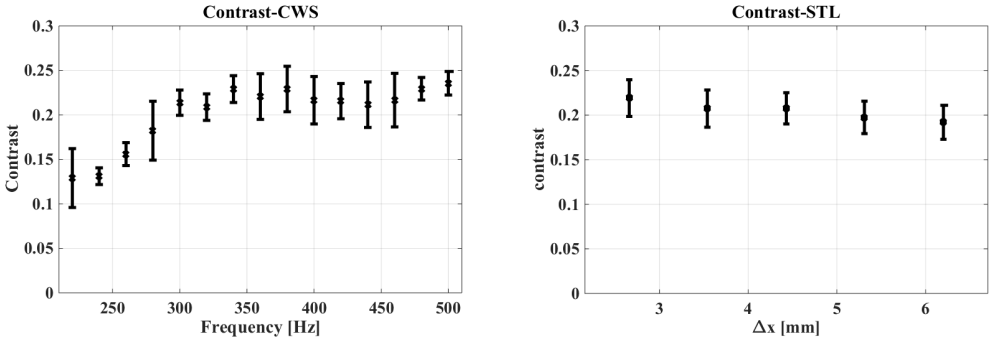

(a) (b)

Figure 4.12: Contrast vs frequency using CWS (left column). Contrast vs Δx using STL-ARFI (right column)

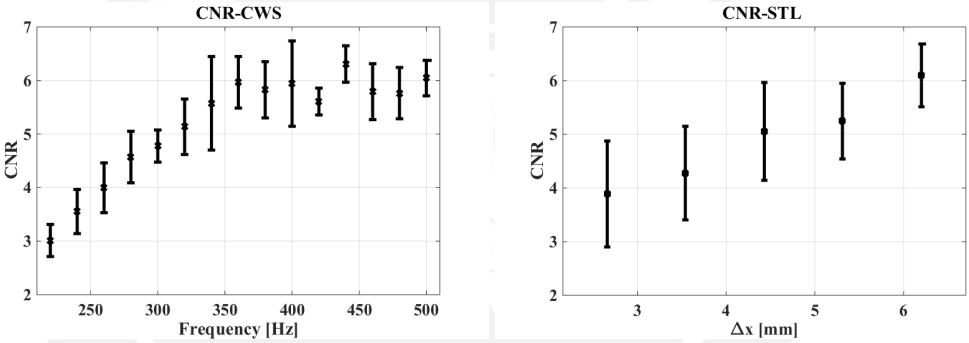

(a) (b)

Figure 4.13: CNR vs frequency using CWS (left column). CNR vs Δx using STL-ARFI (right column)

Chapter 5

Discussion

5.1 SWS and accuracy estimation

Both techniques, CWS and STL-ARFI, are able to estimate SWS in gelatin phantoms developed for this study. For CWS, good correlation was obtained in comparison with results from MM. An accuracy error was found between [0.03%-2.52%] for vibration frequencies between 160 Hz and 500 Hz. For low frequencies, CWS shows larger standard deviations (higher for stiffer materials) which may be explained by the presence of border reflections and longer shear wavelengths. In addition, the combination of lower frequencies and stiffer materials provides the worse condition for SWS estimation using CWS. For STL-ARFI, good correlation was obtained with MM results for a higher frequency range than the used in CWS. The accuracy error was found between [0.01%-6.22%] for all gelatine phantoms. In the latter modality, in order to obtain the SWS *vs*. Frequency data, equation (2.26) and (2.17) were used. The derivation of (2.26) considers a plane wave propagation behavior in the far field for the shear waves generated by the two pushes. More details in the estimation of mechanicals properties in the near and far field using STL-ARFI can be found in [45].
The SWS estimation using CWS and STL-ARFI presents some complementarity, since CWS provide more accurate information for lower frequencies than STL-ARFI. On the other hand, for higher range of frequencies, STL-ARFI could provide information where CWS can not be used due to the presence of higher attenuation in crawling waves as the vibration frequency increased. Additionally, STL-ARFI has the advantage that is not time consuming as CWS because it could provide SWS results for different frequencies using the acquired data in one experiment. Moreover, the SWS values obtained with both elastography modalities are similar to those reported in the literature from tissue mimicking phantoms (2m/s - 6.5m/s) [9]-[48].

5.2 Lateral resolution estimation

With respect to lateral resolution, CWS presents better results (lower resolution values) when the vibration frequency increases. This is expected since shear waves have smaller spatial wavelengths. For STL-ARFI, the lateral resolution was evaluated changing the distance between the push beams ($P1$ and $P2$) to see how much the lateral resolution changes

modifying Δx. It was found that as Δx increases, the lateral resolution has worse performance as expected (see Fig.4.11.b). It can also be noted that, STL-ARFI could obtain comparable lateral resolution results with CWS. Table 5.1 shows lateral resolution values using different elastographic modalities and the results obtained with CWS and STL-ARFI. The lateral resolutions obtained by SWE, ARFI and Strain elastography were better than the ones presented by CWS and STL-ARFI. However ARFI and Strain elastography are qualitative modalities and they can not give elasticity information as CWS and STL-ARFI do. Additionally, Table 5.2 presents the STL-ARFI lateral resolution results compared with the values reported by Rouze et al. [47]. Rouze et al. evaluated the influence of some parameters, like the kernel size (k) for SWS estimation or the excitation beamwidth, in the estimation of the lateral resolution, contrast and CNR using ARF. The results presented in Table 5.2 corresponds to lateral resolution estimation using a kernel size (k) of 3 mm (left column) for ARF [47] and Δx= 2.66 mm for STL-ARFI. As can be seen, the lateral resolution result reported in [47] is better than the obtained with STL-ARFI. However, STL-ARFI can achieve better lateral resolutions decreasing Δx. In that sense,the minimum lateral resolution from STL-ARFI is limited by its beamwidth.

Table 5.1: Comparison with other elastography modalities

Modality \ Parameter	SWE [4]	ARFI [4]	STRAIN	VE [49]	CWS	STL-ARFI
Resolution [mm]	1.10	0.56	2.0 @k=3mm 2.5 @k=4mm [50]*	—	2.38±0.51 @340Hz	2.45±0.76 @Δx=2.66 mm
Contrast	0.56	0.30	—	—	0.92 @340Hz	0.88 @Δx=2.66 mm
CNR	3.50	1.84	3.39 [51]	10.25± 12.83	5.57± 0.87 @340Hz	3.89±0.99 @ Δx=2.66 mm

* k:kernel

5.3 Contrast estimation

For contrast results, CWS shows a contrast increasing when vibration frequencies goes up to 340 Hz, then, contrast almost remains constant for a frequency range between 340 Hz and 500 Hz. This is expected since the ideal contrast is 0.25 considering nominal SWS values of 5 m/s and 4m/s for the inclusion (stiffer region) and background (softer) respectively. For STL-ARFI, the contrast results shows reasonable and comparable values to the ones obtained with CWS (See Fig.4.12.a and Fig.4.12.b. However, it presents an opposite tendency

compared with the contrast results in CWS. As Δx increases, the contrast tends to decrease. Additionally, the values obtained with CWS and STL-ARFI are compared with other contrast values reported in the literature for elastographic techniques. In order to show the comparison, each contrast result was normalized respect to its ideal contrast value. Then, it can be observed that CWS and STL-ARFI presents higher normalized contrast respect to the ones reported using SWE and ARFI elastography (See Table 5.1). In Table 5.2, the normalized contrast result using STL-ARFI is better than the ones obtained in [47]. This was expected because the contrast is better using a narrower excitation beamwidth. The aforementioned reasoning can be founded in [47] too.

Table 5.2: Comparison of STL-ARFI with other SWS estimation based on ARF

SWS estimation based on ARF. Time to peak method [47]			STL-ARFI
	F/2 (1.4 mm beamwidth)	F/4 (2.8 mm beamwidth)	F/3.5 (0.8mm beamwidth)
Resolution	1.9±0.9mm @k=3mm	—	2.45±0.76mm @Δx=2.66mm
Contrast	0.27±0.08	0.15±0.01	0.88±0.08 @Δx=2.66mm
CNR	0.60±0.12	0.95±0.13	3.89±0.99 @Δx=2.66mm

5.4 CNR estimation

Using CWS, CNR results increase as the vibration frequency increases until 340 Hz, then, it can be observed that CWS images do not improve their CNR values. For STL-ARFI, higher CNR results are obtained using a longer Δx value. The CNR estimations obtained using CWS and STL-ARFI are higher than the ones presented in ARFI, SWE and Strain elastography (See 5.1). Additionally, CNR results obtained by Vibro Elastography (VE), which is a technique that uses mechanical forces, are presented in Table 5.1. The CNR value obtained in VE is higher than CWS and STL-ARFI. However VE presents higher standard deviations too. CNR values using STL-ARFI were higher than the ones reported in [47] (See Table 5.2) but it also presents higher standard deviations.

5.5 Lateral resolution, contrast and CNR - summary

In CWS, better lateral resolution, contrast and CNR results were obtained as the vibration frequency increases. It can be seen that for vibration frequencies higher than 340 Hz, CWS presents better lateral resolution, contrast and CNR results than the obtained with STL-ARFI using Δx higher than 4 mm. However, in *in vivo* tissue the attenuation is higher than the one founded in the phantoms used in this study. Thus, the SWS estimation will be harder

for higher vibration frequencies. Considering another studies for in *in vivo* tissue as Zhang et al [1], it can be seen that no higher vibration frequencies than 300 Hz were used. Therefore, taking this last value as a reference of maximum operating vibration frequency, the lateral resolution results, obtained with CWS, are comparable with the ones obtained using STL-ARFI for Δx values among 3 mm and 6 mm. Nevertheless, the contrast and CNR are lower than the obtained with STL-ARFI for the aforementioned range of Δx.

In STL-ARFI, better lateral resolution and contrast were found as Δx decreases its value. However, worse CNR were obtained. Additionally, the application of STL-ARFI in *in vivo* tissue will be limited by the attenuation too. Since the losses are worse increasing Δx, it will be harder to track the induced shear waves. In [45], a liver study was performed using a Δx equal to 5.31 mm. Considering the lateral resolution, contras, CNR results and the Δx value used in [45], it can be said that comparable and reasonable SWS estimations will be obtained applying a Δx range among 3 mm and 6 mm.

Additionally, some recommendations may be given as a consequence of this project. It may be recommended to work in the same environment. Although, the phantom temperature was carefully controlled to keep it constant, some temperature variations could not be avoided because the phantom transportation from one laboratory to the other one used for experiments. It also important recommend to be very carefully with the vibration sources coupling in CWS experiments. Since an incorrect coupling will not able to generate reasonable crawling waves into the material that is scanning.

Chapter 6

Conclusion

It was possible to compare CWS and STL-ARFI and validated them with MM. It was found that CWS has a better performance for a lower operating frequency range than STL-ARFI. However, STL-ARFI can provide information for higher range of frequencies, which can not be obtained using CWS due to the presence of higher attenuation in crawling waves as the vibration frequency increased. These results suggest that further research may be needed for a more accurate evaluation of SWS estimation for lower frequencies using STL-ARFI.

The lateral resolution, contrast, and CNR could be measured using CWS and STL-ARFI. It can be seen that for vibration frequencies higher than 340 Hz, CWS presents better lateral resolution, contrast and CNR results than the obtained with STL-ARFI using Δx higher than 4 mm. Although, CWS was implemented for a range of frequencies up to 500 Hz, its implementation for *in vivo* tissues would be limited to lower frequency ranges in order to avoid higher wave attenuation. On the other hand, STL-ARFI will be limited by the Δx value since a longer distance between the push beams will cause higher losses in the shear wave too. In that sense, for lower vibration frequencies than 300 Hz and Δx values among 3 mm and 6 mm, CWS and STL-ARFI perform comparable lateral resolution, contrast and CNR results.

Finally, the results of this study contribute to the limited data currently available for comparing elastographic techniques. Especially for comparison information related to elastography modalities that use different type of force to generate shear waves inside the material. Moreover, the methodology implemented in this document may be helpful for future standardization for different elastographic modalities.

Bibliography

[1] Man Zhang, Benjamin Castaneda, Zhe Wu, Priya Nigwekar, Jean V. Joseph, Deborah J. Rubens, and Kevin J. Parker, "Congruence of imaging estimators and mechanical measurements of viscoelastic properties of soft tissues," *Ultrasound in medicine & biology*, vol. 33, no. 10, pp. 1617–1631, 2007.

[2] Benjamin Castaneda, "Extracting information from sonoelastographic images," *Diss. University of Rochester*, 2009.

[3] Benjamin Castaneda, Juvenal Ormachea, Paul Rodríguez, and Kevin J. Parker, "Application of numerical methods to elasticity imaging," *Molecular & cellular biomechanics: MCB*, vol. 10, no. 1, pp. 43–65, 2013.

[4] Stephen Rosenzweig, Mark Palmeri, Ned Rouze, Samantha Lipman, Evan Kulbacki, John Madden, Thomas Polascik, and Kathryn Nightingale, "Comparison of concurrently acquired in vivo 3d arfi and swei images of the prostate," *Ultrasonics Symposium (IUS), 2012 IEEE International*, pp. 97–100, 2012.

[5] Kevin J. Parker, Marvin M. Doyley, and Deborah J. Rubens, "Imaging the elastic properties of tissue: the 20 year perspective," *Physics in medicine and biology*, vol. 56, no. 1, pp. R1, 2011.

[6] Jérémie Fromageau, Jean L. Gennisson, Cédric Schmitt, Roch L. Maurice, Rosaire Mongrain, and Guy Cloutier, "Estimation of polyvinyl alcohol cryogel mechanical properties with four ultrasound elastography methods and comparison with gold standard testings," *Ultrasonics, Ferroelectrics and Frequency Control, IEEE Transactions on*, vol. 54, no. 3, pp. 498–509, 2007.

[7] Javier Brum, Jean L. Gennisson, Thu-Mai Nguyen, Nicolas Benech, Mathias Fink, Mickael Tanter, and Carlos Negreira, "Application of 1-d transient elastography for the shear modulus assessment of thin-layered soft tissue: comparison with supersonic shear imaging technique," *Ultrasonics, Ferroelectrics and Frequency Control, IEEE Transactions on*, vol. 59, no. 4, pp. 703–714, 2012.

[8] Hua Xie, Vijay Shamdasani, Heng Zhao, Pengfei Song, Shiwei Zhou, J-L. Robert, James Greenleaf, and Shigao Chen, "A phantom study to cross-validate multimodality shear wave elastography techniques," *Ultrasonics Symposium (IUS), 2012 IEEE International*, pp. 1858–1861, 2012.

[9] Jean L. Gennisson, Alba Marcelan, Alexandre Dizeux, and Mickael Tanter, "High frequency rheology of hybrid hydrogels using ultrasound transient elastography," *Ultrasonics Symposium (IUS), 2012 IEEE International*, pp. 2525–2528, 2012.

[10] Heldmuth Latorre-Ossa, Jean L. Gennisson, Emilie De Brosses, and Mickael Tanter, "Quantitative imaging of nonlinear shear modulus by combining static elastography and shear wave elastography," *Ultrasonics, Ferroelectrics and Frequency Control, IEEE Transactions on*, vol. 59, no. 4, pp. 833–839, 2012.

[11] Jennifer Oudry, Ted Lynch, Jonathan Vappou, Laurent Sandrin, and Véronique Miette, "Comparison of four different techniques to evaluate the elastic properties of phantom in elastography: is there a gold standard?," *Physics in medicine and biology*, vol. 59, no. 19, pp. 5775, 2014.

[12] Kishore Kumar, Maneesha E. Andrews, V. Jayashankar, Ashok K. Mishra, and S. Suresh, "Measurement of viscoelastic properties of polyacrylamide-based tissue-mimicking phantoms for ultrasound elastography applications," *Instrumentation and Measurement, IEEE Transactions on*, vol. 59, no. 5, pp. 1224–1232, 2010.

[13] Robert M. Lerner, Kevin J. Parker, Jarle Holen, Raymond Gramiak, and Robert C. Waag, "Sono-elasticity: medical elasticity images derived from ultrasound signals in mechanically vibrated targets," *Acoustical imaging*, pp. 317–327, 1988.

[14] Jonathan Ophir, Ignacio Cespedes, Hm Ponnekanti, Y. Yazdi, and X. Li, "Elastography: a quantitative method for imaging the elasticity of biological tissues," *Ultrasonic imaging*, vol. 13, no. 2, pp. 111–134, 1991.

[15] Armen P. Sarvazyan, Oleg V. Rudenko, Scott D. Swanson, Brian J. Fowlkes, and Stanislav Y. Emelianov, "Shear wave elasticity imaging: a new ultrasonic technology of medical diagnostics," *Ultrasound in medicine & biology*, vol. 24, no. 9, pp. 1419–1435, 1998.

[16] Mostafa Fatemi and James F. Greenleaf, "Vibro-acoustography: An imaging modality based on ultrasound-stimulated acoustic emission," *Proceedings of the National Academy of Sciences*, vol. 96, no. 12, pp. 6603–6608, 1999.

[17] Stefan Catheline, Francois Wu, and Mathias Fink, "A solution to diffraction biases in sonoelasticity: the acoustic impulse technique," *The Journal of the Acoustical Society of America*, vol. 105, no. 5, pp. 2941–2950, 1999.

[18] Kathryn Nightingale, Roger Nightingale, Mark Palmeri, and Gregg Trahey, "Finite element analysis of radiation force induced tissue motion with experimental validation," *Ultrasonics Symposium, 1999. Proceedings. 1999 IEEE*, vol. 2, pp. 1319–1323, 1999.

[19] Zhe Wu, Lawrence S. Taylor, Deborah J. Rubens, and Kevin J. Parker, "Sonoelastographic imaging of interference patterns for estimation of the shear velocity of homogeneous biomaterials," *Physics in medicine and biology*, vol. 49, no. 6, pp. 911, 2004.

[20] Jeremy Bercoff, Mickael Tanter, and Mathias Fink, "Supersonic shear imaging: a new technique for soft tissue elasticity mapping," *Ultrasonics, Ferroelectrics and Frequency Control, IEEE Transactions on*, vol. 51, no. 4, pp. 396–409, 2004.

[21] Emre Turgay, Septimiu Salcudean, and Robert Rohling, "Identifying the mechanical properties of tissue by ultrasound strain imaging," *Ultrasound in medicine & biology*, vol. 32, no. 2, pp. 221–235, 2006.

[22] Stephen A. McAleavey, Manoj Menon, and Jarrod Orszulak, "Shear-modulus estimation by application of spatially-modulated impulsive acoustic radiation force," *Ultrasonic imaging*, vol. 29, no. 2, pp. 87–104, 2007.

[23] Pengfei Song, Heng Zhao, Armando Manduca, Matthew W. Urban, James F. Greenleaf, and Shigao Chen, "Comb-push ultrasound shear elastography (cuse): a novel method for two-dimensional shear elasticity imaging of soft tissues," *Medical Imaging, IEEE Transactions on*, vol. 31, no. 9, pp. 1821–1832, 2012.

[24] Etana C. Elegbe and Stephen A. McAleavey, "Single tracking location methods suppress speckle noise in shear wave velocity estimation," *Ultrasonic imaging*, vol. 35, no. 2, pp. 109–125, 2013.

[25] Kevin J. Parker and Robert M. Lerner, "Sonoelasticity of organs: shear waves ring a bell," *Journal of ultrasound in medicine*, vol. 11, no. 8, pp. 387–392, 1992.

[26] Benjamin Castaneda, Kenneth Hoyt, M. Zhang, D. Pasternack, L. Baxter, P. Nigwekar, A. di Sant'Agnese, J. Joseph, J. Strang, Deborah J. Rubens, and Kevin J. Parker, "Prostate cancer detection based on three dimensional sonoelastography," *Ultrasonics Symposium, 2007. IEEE*, pp. 1353–1356, 2007.

[27] Lawrence S. Taylor, Deborah J. Rubens, Brian C. Porter, Zhe Wu, Raymond B. Baggs, P. Anthony di Sant'Agnese, Gyongyi Nadasdy, David Pasternack, Edward M Messing, Priya Nigwekar, and Kevin J. PArker, "Prostate cancer: Three-dimensional sonoelastography for in vitro detection 1," *Radiology*, vol. 237, no. 3, pp. 981–985, 2005.

[28] Deborah J. Rubens, Kenneth Hoyt, and Kevin J. Parker, "Sonoelastographic shear velocity imaging: experiments on tissue phantom and prostate," *Ultrasonics Symposium, 2006. IEEE*, pp. 1686–1689, 2006.

[29] Liana Gheorghe, Speranta Iacob, and Cristian Gheorghe, "Real time sonoelastography a new application in the field of liver disease," *J. Gastrointestin Liver Dis.*, vol. 17, no. 4, pp. 469–474, 2008.

[30] Hasan Yerli, Tugbahan Yilmaz, Tolga Kaskati, and Huseyin Gulay, "Qualitative and semiquantitative evaluations of solid breast lesions by sonoelastography," *Journal of Ultrasound in Medicine*, vol. 30, no. 2, pp. 179–186, 2011.

[31] Gianfranco Scaperrotta, Claudio Ferranti, Claudia Costa, Luigi Mariani, Monica Marchesini, Laura Suman, Cristina Folini, and Silvana Bergonzi, "Role of sonoelastography in non-palpable breast lesions," *European radiology*, vol. 18, no. 11, pp. 2381–2389, 2008.

[32] Deborah J. Rubens, Mark A. Hadley, Sheik Kaisar Alam, Lan Gao, Robert D. Mayer, and Kevin J. Parker, "Sonoelasticity imaging of prostate cancer: in vitro results.," *Radiology*, vol. 195, no. 2, pp. 379–383, 1995.

[33] Joyce McLaughlin, Daniel Renzi, Kevin J. Parker, and Zhe Wu, "Shear wave speed recovery using moving interference patterns obtained in sonoelastography experiments," *Journal of the Acoustical Society of America*, vol. 121, no. 4, pp. 2438–2446, 2007.

[34] Kenneth Hoyt, Kevin J. Parker, and Deborah J. Rubens, "Real-time shear velocity imaging using sonoelastographic techniques," *Ultrasound in medicine & biology*, vol. 33, no. 7, pp. 1086–1097, 2007.

[35] Kenneth Hoyt, Benjamin Castaneda, and Kevin J. Parker, "Two-dimensional sonoelastographic shear velocity imaging," *Ultrasound in medicine & biology*, vol. 34, no. 2, pp. 276–288, 2008.

[36] Kenneth Hoyt, Benjamin Castaneda, and Kevin J. Parker, "5c-6 muscle tissue characterization using quantitative sonoelastography: Preliminary results," *Ultrasonics Symposium, 2007. IEEE*, pp. 365–368, 2007.

[37] Kenneth Hoyt, Timothy Kneezel, Benjamin Castaneda, and Kevin J. Parker, "Quantitative sonoelastography for the in vivo assessment of skeletal muscle viscoelasticity," *Physics in medicine and biology*, vol. 53, no. 15, pp. 4063–4080, 2008.

[38] Brian S. Garra, Ignacio E. Cespedes, Jonathan Ophir, Stephen R. Spratt, Rebecca A. Zuurbier, Colette M. Magnant, and Marie F. Pennanen, "Elastography of breast lesions: initial clinical results," *Radiology*, vol. 202, no. 1, pp. 79–86, 1997.

[39] L. Curiel, R. Souchon, O. Rouviere, A. Gelet, and J.Y. Chapelon, "Elastography for the follow-up of high-intensity focused ultrasound prostate cancer treatment: initial comparison with mri," *Ultrasound in medicine & biology*, vol. 31, no. 11, pp. 1461–1468, 2005.

[40] Raffaella Righetti, Faouzi Kallel, Jason R. Stafford, Roger E. Price, Thomas A. Krouskop, John D. Hazle, and Jonathan Ophir, "Elastographic characterization of hifu-induced lesions in canine livers," *Ultrasound in medicine & biology*, vol. 25, no. 7, pp. 1099–1113, 1999.

[41] Tomy Varghese, Udomchai Techavipoo, Wu Liu, James A. Zagzebski, Quan Chen, Gary Frank, and Fred T. Lee Jr., "Elastographic measurement of the area and volume of thermal lesions resulting from radiofrequency ablation: pathologic correlation," *American journal of roentgenology*, vol. 181, no. 3, pp. 701–707, 2003.

[42] GR. Torr, "The acoustic radiation force," *American Journal of Physics*, vol. 52, no. 5, pp. 402–408, 1984.

[43] Allison Y. Iyo, "Acoustic radiation force impulse imaging: a literature review," *Journal of Diagnostic Medical Sonography*, vol. 25, no. 4, pp. 204–211, 2009.

[44] Stephen McAleavey, Erin Collins, Johanna Kelly, Etana Elegbe, and Manoj Menon, "Validation of smurf estimation of shear modulus in hydrogels," *Ultrasonic imaging*, vol. 31, no. 2, pp. 131–150, 2009.

[45] Jonathan H. Langdon and Stephen A. McAleavey, "Single track location viscosity estimation by maximum likelihood estimation," *Ultrasonics Symposium (IUS), 2014 IEEE International*, pp. 991–996, 2014.

[46] Zaegyoo Hah, Chris Hazard, Bradley Mills, Christopher Barry, Deborah J. Rubens, and Kevin J. Parker, "Integration of crawling waves in an ultrasound imaging system. part 2: signal processing and applications," *Ultrasound in medicine & biology*, vol. 38, no. 2, pp. 312–323, 2012.

[47] Ned C. Rouze, Michael H. Wang, Mark L. Palmeri, and Kathryn R. Nightingale, "Parameters affecting the resolution and accuracy of 2-d quantitative shear wave images," *Ultrasonics, Ferroelectrics and Frequency Control, IEEE Transactions on*, vol. 59, no. 8, pp. 1729–1740, 2012.

[48] Anna Maeva, Malrey Lee, and Stuart Foster, "Shear wave imaging at high frequencies: A feasibility study in tissue mimicking gelatin phantoms," *Ultrasonics Symposium (IUS), 2012 IEEE International*, pp. 2552–2554, 2012.

[49] S. Sara Mahdavi, Mehdi Moradi, Xu Wen, William J. Morris, and Septimiu E. Salcudean, "Evaluation of visualization of the prostate gland in vibro-elastography images," *Medical image analysis*, vol. 15, no. 4, pp. 589–600, 2011.

[50] S. Srinivasan, R. Righetti, and Jonathan Ophir, "An experimental characterization of spatial resolution in elastography: analysis of the tradeoffs between spatial resolution and contrast-to-noise ratio," *Ultrasonics, 2003 IEEE Symposium on*, vol. 2, pp. 1618–1621, 2003.

[51] Hassan Rivaz, Emad M. Boctor, Michael A. Choti, and Gregory D. Hager, "Ultrasound elastography using three images," *Medical Image Computing and Computer-Assisted Intervention–MICCAI 2011*, pp. 371–378, 2011.